L. Giacomelli, C. Hellesen, A. Hjalmarsson, H. Sjöstrand, J. Källne, S. Conroy, G. Ericsson, E. Andersson Sundén, M. Gatu Johnson, W. Glasser, G. Gorini, E. Ronchi, M. Tardocchi, M. Weiszflog and JET EFDA contributors

Characterization of Phoswich Scintillation Detectors for the Focal Plane Hodoscope of Magnetic Proton Recoil Spectrometers for Fusion Neutrons

Characterization of Phoswich Scintillation Detectors for the Focal Plane Hodoscope of Magnetic Proton Recoil Spectrometers for Fusion Neutrons

L. Giacomelli[1], C. Hellesen[1], A. Hjalmarsson[1], H. Sjöstrand[1], J. Källne[1], S. Conroy[1], G. Ericsson[1], E. Andersson Sundén[1], M. Gatu Johnson[1], W. Glasser[1], G. Gorini[2], E. Ronchi[1], M. Tardocchi[2], M. Weiszflog[1] and JET EFDA contributors*

JET-EFDA, Culham Science Centre, OX14 3DB, Abingdon, UK

[1]*Department of Neutron Research, Uppsala University, EURATOM-VR Association, Uppsala, Sweden*
[2]*Department of Physics, University of Milano-Bicocca and Istituto di Fisica del Plasma, EURATOM-ENEA-CNR Association, Milano, Italy*
* See annex of M.L. Watkins et al, "Overview of JET Results ",
(Proc. 21st IAEA Fusion Energy Conference, Chengdu, China (2006)).

ABSTRACT

Phoswich scintillators have been tested for use in the focal plane detector of the Magnetic Proton Recoil (MPR) spectrometer for measurement of neutrons over the energy range 1.5 to 18MeV emitted from fusion plasmas created in the JET tokamak. The tests were performed on prototypes to detect protons over an area of 90×10 mm^2 with two layers of 0.3 and 2.5 mm thickness of fast and slow decay times with PM tubes attached to one or both ends; comparison were made with MPR monolithic scintillators. The tests were performed with a and b radiation sources besides with accelerator beam protons to measure the waveforms of the pulses generated in either or both the scintillator layers depending on the range of the radiation. The purpose of the test was to determine the efficiency of using pulse shape as a mean to identify protons of different energies and the accuracy by which this could be done in order to achieve effective separation from background radiation. The pulse shape was represented as the integrated early and late periods of the waveforms (A1 and A2) where the protons appear well localized compared to the spread-out background events. The results were used to define the design for construction of the phoswich hodoscope as the main part of the upgrade of the spectrometer (MPRu) and to characterize its performance under the measurement conditions at JET. The performance of the phoswich scintillators as installed in the MPRu is also presented based on initial measurements at JET.

1. INTRODUCTION

The neutron emission carries information about the motional state of the fuel ions in fusion plasmas which is derived from different types of neutron diagnostic measurements. The most detailed information comes from Neutron Emission Spectroscopy (NES) diagnostic which has a long history of fusion plasma studies with tokamaks. Here JET has been leading the NES development since its start of operation in 1983 [1]. A milestone was passed in 1997 when JET carried out its first main Deuterium Tritium Experiment (DTE1) reaching a record 14-MeV neutron yield rate of d+t→a+n reactions. This offered a special opportunity for NES studies which was exploited with the Magnetic Proton Recoil (MPR) neutron spectrometer installed at JET in 1996 [2,3,4]. The MPR produced a number of new results, especially on the effects of auxiliary heating using radio frequency [5] and neutral beam sources [6] as well as the observations of a particles [7]. After DTE1, JET went back to operation with tritium in 2003 with the Trace Tritium campaign (TTE) with a strict neutron production limit. Some additional new results were obtained [8, 9]. While the MPR had demonstrated NES diagnostic results of unsurpassed quality for 14MeV neutrons it had also shown weakness in measurements of 2.5MeV neutrons which impeded the diagnosis of deuterium plasmas. In other words, the MPR needed further development for use as a diagnostic instrument also for deuterium plasmas which are the most frequently used in fusion studies with tokamaks.

The MPR spectrometer is based on the measurement of the proton recoils from neutron head-on scattering in a polyethylene target [10]. The protons passing through the magnet are detected at the exit focal plane in an array (hodoscope) of plastic monolithic scintillators [11] each coupled to a

Photo Multiplier (PM) tube. The hodoscope was optimized for 14MeV neutrons. This means that the thickness of the scintillators was chosen so as to stop recoil protons up to $E_n \approx 18MeV$. The detector was also required to provide good background rejection in measurements of the 14MeV dt neutron emission from DT plasmas, i.e., a signal to background ratio of $S/B \approx 10^4$. It was also tested in measurements of 2.5MeV neutrons from $d + d \rightarrow {}^3He + n$ but found to provide insufficient background rejection with an estimated $S/B \approx 10^{-1}$ [12]. The main cause of the low S/B value was identified to be Compton electrons in the MeV range passing through the scintillators producing pulses of similar amplitude to those of 2.5MeV protons. It was therefore decided to develop a new MPR focal plane detector which could provide adequate background rejection in measurement of recoil protons for the fusion neutron energy range of interest, i.e., $E_n = 1.5$ to 18MeV. The new focal plane became the main part of the project to upgrade the MPR (MPRu) [13,14].

This paper describes the tests performed on phoswich prototype detectors to determine the design of the new MPRu focal plane detectors to meet the requirements of good signals for protons of energies around both 2.5 and 14 MeV and high background immunity (i.e., S/B ratio). In other words, the overall goal of the MPRu project was to provide an instrument for neutron emission spectroscopy diagnosis of both D and DT plasmas in the upcoming experimental campaigns at JET in 2006 and beyond. It was early identified that a possible solution would be to use phoswich scintillators [14]. These consist of laminated layers of similar optical properties but a suitable difference for shape of the light pulses emitted in response to ionizing radiation. The underlying idea behind the use of the phoswich technique is that the light produced can be identified as originating in the first layer (L1) facing the incoming protons or both layers L1 and L2 based on the measured shape of the pulse which is recorded by a PhotoMultiplier (PM) tube viewing both layers. In other word, the phoswich scintillators of the MPRu focal plane detectors would allow one to identify radiation based on range besides pulse height. Specifically, the thickness of the layers should be chosen with respect to the range of dd and dt neutron proton recoils. The practical choice for the project implied L1 0.3mm thick and a total thickness L1+L2 of about 3mm for dt incoming neutrons up to about 18 MeV.

Although the phoswich technique has been used earlier in several applications, a special practical requirement for the MPR application is the use of elongated scintillators (about $0.3 \times 1 \times 10$ cm^3) with PM tubes attached to both ends to achieve high light collection efficiency. This arrangement was therefore a special objective of the tests. For their utilization at JET, the phoswich detectors made it necessary to record the shape of pulses at rates at a few tens of kHz. This problem was solved by the development of PCI Transient Recorder (TR) cards [15]. These were designed specifically for the MPRu and provided accurate digitization of the pulse shapes (waveforms) so the uncertainties in the pulse identification data derived predominantly from photoelectron statistics of the PM tube pulse besides noise.

The tests were performed at low event rates where waveforms were recorded with an oscilloscope offering sampling rates up to 500MHz compared to 200MHz of the TR cards. The tests reported

here include the use of a and b radiation sources besides accelerator beams of protons of variable energy. The methods used are described and the results obtained are presented in the perspective of their implications for the proton identification and background separation under conditions of operation on JET. It is also discussed how the results of the tests have been implemented in the design of MPRu focal plane detector and how they have provided inputs for the reduction of the data taken in the neutron emission spectroscopy experiments with the MPRu at JET.

2. EXPERIMENTAL TESTS OF THE DETECTOR PROTOTYPES

The phoswich prototype detectors were made of scintillators producing a fast (1.8ns decay time) and slow (179.7ns) light pulses in response to ionizing radiation, i.e., a thin layer L1 and a thicker layer L2 of the materials Bicron BC-404 and BC-444. The light peak emission occurs at different wavelengths (λ = 408 and 428 nm) with a difference in relative light yield of 1:0.6 but with the same index of refraction and optical and physical characteristics as summarized in Tables 1 and 2 [16]. Some phoswich scintillators had a third layer of acrylic plastic (Bicron BC-800) used as backing (b) to improve the light transport along the scintillator strip (Table 2); it has an index of refraction near that of the scintillators, i.e., 1.58 compared to 1.49.

The detectors in the tests made use of three different types of scintillators of the dimensions shown in Table 3. The prototype phoswich scintillators were of two kinds, without (P) and with (P/ b) backing. The monolithic ones (M of BC-404 material) differed by thickness (3.5 and 2.8mm) and width (20 and 8mm) for M1 and M2, respectively, and are 100mm long. This can be compared with a thickness of 2.8mm for the prototypes, and lengths and widths of 90 and 10mm. In Table 3 is also listed the small scintillator used in b coincidence measurements (referred to as the C detector). Moreover, the prototypes can be compared with the phoswich scintillators that were finally constructed for installation in MPRu (Table 4).

The scintillators were coupled to PM tubes via light guides of different geometry, cylindrical and of fishtail type. Photographs of prototype and MPR detector assemblies are shown in Fig.1.

Two kinds of PM tubes were used, namely, Hamamatsu R647-25MOD (H) or ElectronTube JET A PV19VN-06 (E) with a photo cathode diameter of 13 and 16.5mm, respectively. These were coupled to the light guides at one or both of the short ends of the scintillator. They have a gain of about 10^6 for applied maximum voltages of 1250 and 1550V. The PM tubes have a bialkali photo cathode sensitive to wavelengths in the range about 300-600nm with the maximum quantum efficiency peak of 0.25-0.30 at about 400nm matching the scintillator light emission. A single H type PM tube was used for each scintillator in the MPR detector and the E type was implemented on the MPRu with two PM tubes coupled to each scintillator end.

The tests aimed at the characterization of the phoswich detector prototypes with respect to the pulse shape difference of signals coming from the scintillator layers and/or induced by different ionizing radiation, to the pulse height resolution and light transport and, ultimately, to verify their behaviour in setup mimicking the final operative conditions at JET. The radiation used consists in

α and β emitting sources besides proton (p) beams of different energy.

The α source consisted of ^{241}Am deposited on a metal support with an activity of 5kBq and the main emission at E_{α} = 5.5MeV. The source was placed facing the scintillator surface but at a slight distance so as to avoid contact.

The β radiation was obtained from ^{106}Ru which decays $^{106}_{44}$Ru → $^{106}_{45}$Rh → $^{106}_{46}$Pd.DSMT4 with half-lives of 373.59 d and 29.80s and accompanied β emission with end point energies of 0.039MeV and 3.541MeV, respectively. ^{106}Rh is also a γ emitter with principal line energies of 0.51MeV (20.4%), 0.62MeV (9.9%) and 1.05MeV (1.6%) [17]. There are other contributions of higher energy, up to 2.3MeV, but lower in intensity by two orders of magnitude. The source is deposited on a thin disc, 1-mm thick and 13.6-mm diameter, with a specific activity of 2MBq/cm^2 and placed in a shielding from which the electron emission was taken out as a beam through a 2mm opening [18]. The collimated β source was used together with the coincidence C detector so as to define the b's passing the test scintillator as minimum ionizing radiation (β_{min}). The system of the β source and the C detector was mounted on an xy-table controlled with a computer. The x motion was set with a computer controlled motor with a precision of 1/80mm. In another test the source was used without collimation just to irradiate the test scintillator directly.

The proton tests were performed at the Tandem Accelerator of the Ångström Laboratory in Uppsala with beams of selected energies in the range 1 to 7MeV to an accuracy of ΔE/E~0.1 %. The beam was passed through a collimator (750mm long and 5mm diameter) directed to the test scintillator placed 30cm downstream in a vacuum chamber of 80cm diameter at 2×10^{-6} mbar. These tests were meant to simulate the focal plane conditions of the MPRu so the scintillator was of the P/β type (see below) wrapped in 6-mm aluminum foil with the fast scintillator L1 facing the beam.

With the α, β and proton sources one can test various characteristics of the scintillators exploiting their differences in light yield and range [19]. The ranges are such that the 5.5MeV α's stop in the thin L1. This is also true for protons of E_p up to ≈5MeV and β's of E_{β}<0.06MeV while those of higher energy can reach L2. b's of E_b>0.6 MeV would pass through both layers. These examples refer to incident radiation perpendicularly into L1 and a similar situation also applies to recoil protons impinging on the MPRu focal plane.

The relative light yield curves as function of energy produced by β's, protons, deuterons and α's stopping in a plastic scintillator are shown in Fig.2. The tests are summarized in Table 5. Two experiments (3 and 7) used two different detectors for comparative studies and are marked a and b.

Tests 1 and 2 used the a source placed in the center of the scintillator for general waveforms studies (Fig.3). The responses of the BC-404 and BC-444 were compared in test 1 using detector P while the effect of the backing was studied by comparing the results of tests 1 and 2 on P and P/b. In test 3, the source was placed at different positions of the scintillator, i.e., the near and far ends relative to the PM tube (Fig.4). The aim was to study the attenuation of the light transport and how it differed between the P/b phoswich and M1 monolithic scintillators (a and b). Test 4 was done with a similar setup to that of test 2 but to study cable transmission effects on the pulse shape by varying the cable length.

Test 5 entailed the use of the b source in the setup with the coincidence detector C which was required to produce a minimum signal of 0.6MeV (Fig.5). The aim of the setup was to provide minimum ionizing electrons passing through the test scintillator with a specific energy loss, 2MeV/(g cm^{-2}) [19], and energy disposition proportional to the traversed distance. Since the C detector was of small dimension it also helped to define the radiated area of the test scintillator. The source and C-detector system was placed on an xy-table and moved to selected positions set by computer control. These measurements were carried out to determine the light response of the test scintillators for known energy deposition at different longitudinal positions.

Test 6 was carried out with the accelerator proton beam of small spot size (φ<1cm) aimed at the scintillators center (Fig. 6). The data acquisition system was at a cable length distance of about 20m. The beam was set to eight different energies. A slight energy degradation of protons impinging the scintillator was due to the Al foil wrapping (Table 6). The odd value of 4.7MeV was chosen as it corresponds to the range of the L1 layer. The data collected consisted of 2×10^3 to 4×10^3 waveforms for the eight energies as summarized in Table 6.

Experiment 7 aimed at testing the response difference of the BC-404 scintillator in P/b and M2 and its dependence on type of ionizing radiation (α and β); the same PM tube and electronics were used in the test to allow detailed comparisons of the data sets. For the a's the measured pulse height distribution reflects a weak scattered, energy degraded, component besides the main full 5.5MeV component. In the case of β's, the deposited energy in the scintillator depends on the distance traveled through the scintillator. This means that the β data recorded with the P/b detector contain some events due to energy deposition in BC-404 layer only which can be selected based on their waveforms. Moreover, the energy deposition can range from zero up to beyond that of 5.5MeV α's corresponding to 0.4MeV (cf. Fig.2). In order to study the waveform shapes in detail, the digital oscilloscope was set to the sampling rate of 2.5GHz (time steps of 0.4ns) over the interval −39.6 to 160ns; a short (3m) RG-58 cable was used to connect it to the PM tube.

The data acquisition system made use of a computer and a digital oscilloscope (Tektronix TDS 3034) run over the Internet, with the communication software TekVISA V2.03 [21] and a purpose written program for the data read out and processing. The PM tube signals were fed into the oscilloscope which digitized them into waveforms with a 10-bit amplitude resolution and sampling frequency of 1 or 2.5GHz depending on requirements. In cases of two PM tubes, one was used to trigger the oscilloscope acquisition and define the reference time for the waveforms. The trigger pulse was selected by a threshold discriminator set at low values, namely, 10-20% of the maximum pulse height to minimize the pulse height walk. In experiment 7, where very low amplitude signals were studied, a threshold discriminator still produced the trigger signal and pulse height walk correction was performed in the off line analysis. In experiment 5, pulses from the coincidence detector C defined the trigger. The amount of data collected was adjusted to the statistical requirements for the tests to be performed which meant the range 2×10^3 to 2×10^4 for experiments 1 to 6, and 6×10^4 to 1.4×10^5 in experiment 7.

3. DATA, REDUCTION METHODS AND EXTRACTED INFORMATION

The data for individual pulses were recorded and stored as waveforms, i.e., voltage amplitudes values as function of time, P(t). The shape was parameterized as amplitudes A1 and A2 obtained by integrating P(t) over the time ranges G1 and G2 normally defined by the limits -4 to 60ns, and 60 to 460ns (Fig. 7) [22]. The amplitude A1 thus reflects the integrated pulse for the main part of signals from the fast scintillators of the BC-404 type and the early part of signals from BC-444. The amplitude A2 contains a relatively large fraction of the BC-444 pulses because of their long decay time (179.7ns). Moreover, the gate G3, with limits -12 to 700ns, was used to determine A3 which is the integrated amplitude value for the full waveform. The A3 parameter was also used for standard analysis of the data. In addition, the gate G0 with the limits from -182 to -82ns was used to determine A0. The A0 amplitude represents the integrated base line preceding a pulse from which the baseline level per sampling bin B was determined. The base line correction was routinely applied to the measured data and is included in all presented results.

The gates were normally set relative to the reference time $t = t_o$ where t_o is the time when the leading edge of the waveform passes the trigger level. This method was used in all experiments with two exceptions. In test 5 with the β_{min} source, $t_o = t_C$ was taken from the detector C. This gave somewhat poorer definition of the gate limits but was of little practical consequence for the results as A3 was of most interest in this case. We could also determine the time variation in the signal of the test detector P/b given by $\delta t = t_{P/b} - t_C$. In test 7 instead t_o was determined for each waveform recorded as part of the off line analysis and corresponding to $P(t_o)/P^{max} = 25\%$. This gave an improvement in time alignment of the low amplitude waveforms as illustrated in Fig.8.

The spread of the amplitude distribution depends on the statistical variation in each data set. In addition there is a contribution from the base line correction which was determined from $\sigma_B = \sigma_{noise}/\sqrt{n_B}$ here σ_{noise} is the variation in the noise level causing the base line to assume a certain value and n_B is the number of samples [23]. For instance, for G0 with $n_B = 80$ and $s_{noise} = 1.4$mV as typical values one obtains $s_B = 0.16$mV that was hence incorporated in the ascribed error of the extracted amplitude values A1, A2 and A3.

The accuracy of the pulse shape measurement derives ultimately from the number of photoelectrons N_e produced by scintillation light at the cathode of the PM tube. An experiment would give a distribution of measured amplitude values reflecting the underlying variation in N_e which can be assumed to be Poisson distributed with mean value $N_e = \mu$ and standard deviation $\sigma = \sqrt{\mu}$. The resolution h is determined as the ratio of the measured full width at half maximum (FWHM, W) and the position m of the pulse height (amplitude) distribution, i.e., the resolution is $\eta = W/\mu = 2.355(s/m)$ and $N_e = (\mu/\sigma)^2 = (2.355/\eta)^2$ is the estimated number of photoelectrons.The pulse height resolution of the measurements was normally represented by the results on the A3 distribution. These showed a peak of symmetric shape in the a and proton experiments which was fitted with a Gaussian to extract the desired parameters; an example is shown in Fig.9 for α's with the results $\eta = 48.4$ % and $N_e = 24$.

In the experiments with the scintillators coupled to two PM tubes one can analyze the amplitude distributions of correlated events individually, say $A3_1$ and $A3_2$ (Fig. 11) or as the summed distribution $A3_{1+2}$. These were used to determine corresponding response parameters, i.e., for instance, μ_1 and μ_2 with the sum $\mu_{SUM} = \mu_1 + \mu_2$, and σ_1 and σ_2 with the sum $\sigma_{SUM}^2 = \sigma_1^2 + \sigma_2^2$, and μ_{1+2} and σ_{1+2}. The relationship between the two sets of results depends on the correlation between $A3_1$ and $A3_2$ and is expressed by the covariance function $Cov(A3_1, A3_2)$ through:

$$\sigma_{1+2}^I = \sigma^2(A3_1 + A3_2) = \sigma_{SUM}^2 + 2Cov(A3_1 + A3_2) \tag{1}$$

The correlation can be quantitatively estimated with the Pearson's coefficient $r(x,y)$ given by

$$\rho(x, y) = \frac{\sum_i (x_i - \bar{x})(y_i - \bar{y})}{\sqrt{\sum_i (x_i - \bar{x})^2 \sum_i (y_i - \bar{y})^2}}$$

which was used to analyze the amplitude width results. If the correlation is small one obtains the relationship between the variances of the summed individual distribution given by

$$\sigma_{1+2} \approx \sigma_{SUM} = \sqrt{\sigma_1^2 = \sigma_2^2} \approx \sigma \quad \text{and} \quad \frac{\sigma_{1+2}}{\mu_{1+2}} \approx \frac{1}{2}\sqrt{\left(\frac{\sigma_1}{\mu_1}\right)^2 + \left(\frac{\sigma_2}{\mu_2}\right)^2} \quad \text{if} \quad \mu_1 = \mu_2 = \frac{\mu_{1+2}}{2} \quad \text{and}$$

$$\sigma_{1+2} \approx \sigma\sqrt{2} \quad \text{if} \quad \sigma_1 = \sigma_2 \approx \sigma$$

4. EXPERIMENTAL RESULTS

4.1 ALPHA TESTS

Test 1 with the α source was performed to compare the waveform response of the BC-404 (L1) and BC-444 (L2) layers in the phoswich detector without backing (P). Moreover, the results for L1 were compared with those obtained for P/b in test 2. The data were obtained for PM tubes 1 and 2 individually and were analyzed likewise or after summation (PM1+2); the PM1 signal provided the trigger, thus, setting the reference t_o for the gate limits of both. Summed signals were used to reduce noise interference and statistical fluctuations which impede the observation of waveforms, especially, for the slow signals from α's stopping in L2. Examples are shown in Fig. 12 where α's into L1 give waveforms of well-characterized shape compared to those from L2. The L2 waveforms are barely discernable despite the use of summed PM1+2 pulses because of superimposed noise. Actually, at the low (-7mV) threshold used, it appears that short duration fluctuations can provide triggers rather than the signal waveforms which do not exceed the pulse height limit as they are stretched out in time (see below). There is also some time jitter in the waveforms of the L1 signals due to the statistical nature of the light emission of the scintillator. It is reduced for the P/b detector which can be ascribed to the observed pulse height increase relative to the P detector (Fig.12a and c) due to a corresponding improvement in the light transmission to the PM tubes and increased number of photoelectrons, as will be discussed later. The remedy to fluctuations is to base the pulse shape

analysis on time integrated derived information in terms of A1 and A2 amplitudes (Fig.13).

The figure shows that the α induced events in L1 and L2 appear in different A1-A2 regions for the individual PM tube signals. The L1 events appear with a distribution over a well-confined region as can be expected as we shall discuss later. The L2 event distribution, however, has a tail towards the origin of the plot and even into the unphysical region of negative A1 and A2 values which is uncharacteristic for stopping a's in L2. These non-typical a events are indeed spurious ones that are removed by only considering events of A3 values above threshold of $A3_{th} = 0.03$ a.u. The thus selected events show the expected distribution in the A1-A2 plot (Fig.13b). The events generated by α's in the L1 and L2 layers are even better separated if the summed PM1+2 pulse are used (Fig. 13c) which demonstrates the effect of a factor 2 increase in counting statistics.

The fluctuation in the signal data can be reduced by considering the average waveform for the α events in the two detector layers. The results on the averages recorded with the P detector (Fig.14) show that individual PM1 and PM2 signals are very similar for L1 but conspicuous different for L2 where PM2 shows a waveform with a sharp peak at $t = 2$ ns superimposed on the low and extended distribution common to both waveforms. The peak indicates the time for the trigger which is likely to be caused by a fast fluctuation (cf. Fig.12b) induced by noise occurring during the broad waveform of an a generated event in L2. This means that time t_o for trigger would not be fixed but would show a walk relative to the waveform reflecting the time response of light pulses in L2, i.e., about 180 ns.

The fast contribution in the waveform of PM2 was removed to generate averaged waveforms for the sum PM1+2 to improve the shape definition with the results shown in Fig.14b. The L1 and L2 waveforms show fall times of 10 and 170ns which are in line with the specifications of BC-404 and BC-444 (cf. Table 1). The same is true for the rise time of L1 while the leading edge of the L2 waveform shows seemingly exponential change with time from $t = -70$ ns to its minimum at $t = 0$. This is not reflecting the light pulse characteristics in BC-444 with a rise time of 20ns but the effect of time walk of their triggering point that occurs during a real pulse as mentioned above.

As noted above, the configuration with backing and cylindrical light guides improves the light transport which is further illustrated by the averaged waveforms (Fig. 15) recorded by L1 in the P and P/b detectors. In other words, the results show that the P/b detector features higher pulse height by a factor of about 2.6 with no change in waveform shape.

The A1-A2 representation of the two data sets (Fig.16a) shows two regions with centers approximately on the line of $A1-9A2 = 0$ where the P/b events are moved outward corresponding to their higher amplitude. Otherwise, the two distributions are similar confirming that the waveform shape is unaffected by the backing. If the P events are normalized so that the event populations for P and P/b give the same average amplitude, say in terms of A3, they can be overlaid in the same A1-A2 plot for direct comparison (Fig.16b). One thus finds that the P and P/b detectors show the same event distributions with coinciding centers, but the P events extend over a larger region displaying a greater scatter from the average center. The event scatter is related to pulse amplitudes which, in turn, are connected to the pulse height resolution of the measurement.

8

The pulse height resolution was derived from the distributions of A3 amplitudes as well as from A1 and A2, where possible. These distributions were Gaussian fitted (cf. Fig. 9) to determine the parameters m and h. The resolution $\eta = W/\mu$ is related to the statistical uncertainty connected to the number of photoelectrons through: $N_e = (2.355/\eta)^2$. These A3 results for PM1, PM2 and PM1+2, besides A1 and A2 results for PM1+2, are presented in Table 7. The improvement in light collection efficiency is demonstrated by the resolution of the A3 amplitudes obtained in the tests. The N_e ratios for individual and summed distributions for detectors P/b and P are 2.2 and 2.1, respectively.

The A3 results on m and h derived from individual signals are the same within uncertainties so one can continue to inspect the results for PM1+2. The resolution values for A3 (η_3) can be compared with those of A1 and A2. It was found that the η_1 and η_2 values are systematically higher than the corresponding η_3 values by a factor about $\sqrt{2}$ that would be expected to apply for uncorrelated variables (see below for details). The phoswich detector gives 2.5 higher μ in terms of A3 with backing than without which is in line with the results obtained in the A1-A2 plot of Fig. 16. Still for A3, the μ response of L2 relative to L1 is a factor of 0.6 lower which is expected from the scintillators' light yield ratio. The m values of A1 and A2 are in the ratios of about 9:1 and 1:2 for α's on the L1 and L2 layers, respectively. In principle, the variation in m would be expected to be reflected in N_e, derived from h. Such a systematic can be seen in the results on η but with exceptions. For instance, the A3 distribution for L1 gives a lower N_e value than the A1 distribution although its μ value is lower. Similarly, the A2 distribution gives lower N_e value in comparison to that of A1. However, the underlying assumption for proportionality between N_e and μ is that the resolution is solely determined by photoelectron statistics. This is clearly not the case since there are other effects such as low amplitude pulses and noise that affect the measurement.

The relationship between the resolution values η_1, η_2, η_{1+2}, η_{SUM} were examined with regard to a possible underlying correlation of the signals recorded by PM1 and PM2 tubes using Eq.1. The resolution results for A3 are presented in Table 8 besides the correlation factor ρ. It is found that the η_{1+2} are systematically larger than the value η_{SUM} derived from the quadratic sum of η_1 and h_2. Such difference would indicate a correlation between PM1 and PM2 signals but it may well be inside the uncertainties. The correlation coefficient r is determined to be greater than zero which would indicate a covariance between measured η_1 and η_2. A certain correlation between the amplitudes of the two PM tubes is indicated by their A3 event distributions in the plot (Fig.17) for the cases shown in Table 8.

Here one can see that the peak of the P/b and M1 signals both differ by factor 2 from the near to far source positions relative to the PM tube. The shape of the P/b signal shows a slight dependence on the interaction position compared to M1. However, the striking difference between the P/b and M1 response is preserved (Fig.18b). Specifically, the falling edges show a maximum difference around $t \approx 10$ns to become insignificant beyond $t \approx 60$ns, i.e., the waveform tail of P/b exceeds that for the M1 detector by about 30% of the entire waveform area. The light transmission efficiency of the P/b and M1 detectors was assessed quantitatively in terms of the near/far A3 ratios of 2.4/1.2

and 1.5/0.9, respectively. This indicates a longitudinal amplitude reduction by 50 and 40%, respectively, over a distance of about 7cm (see Fig. 4). Finally, the cable transmission effects on the waveform were studied through measurements of the a signal from L1(P/b) using cables of different lengths in the range $L_C = 0\text{-}120m$ (test 4). The results show that the amplitude decreases with L_C and there is also a gradual change in shape (Fig. 19). The quantitative results on attenuation in terms of relative peak amplitude, rise time and width of the average pulse are presented in Table 9. The frequency dispersive effects of the cable for a length up $L_C = 120$ m are thus found to slow down of the rise time of the pulse from 4 to 8 ns and increase its width from 10 to 30ns.

4.2 BETA TESTS

The detector P/b was mapped in experiment 5 with the β_{min} source in order to determine the longitudinal response dependence of the scintillator. This test was based on five source positions, namely, center and ±20 and ±40mm towards the PM1 (−) and PM2 (+) tubes. The center position was used as a reference that was returned to during the scans to check for measurement stability. Waveforms were determined from PM1, PM2 and PM1+2 signals, as described earlier, besides from PM0 of the coincidence detector C. Examples of results are shown in Fig.20 for the PM1+2 signals of P/b compared with those of PM0 for coincidental P/b-C events where the C events provide the trigger time.

The P/b signals show fluctuations due to statistics and/or noise. The latter can be due to spurious γ's from the source which by chance interact during C detector triggers. These accidental events have been removed from the desired coincidental ones due to β_{min} radiation passing P/b using the waveform data in the A1-A2 parameterized form. Fig. 21 shows events centered around A1 = 0.25 and A2 = 0.4 which can be ascribed to β_{min} based on their location relative to a events. These events can be distinguished from those of lower A1 values identified as spurious as confirmed in the inspection of the correlation between the measured A3 amplitudes with P/b and C detectors (Fig.22).

Here the band of events gathering around $A3_{P/b}$=0.8 a.u. independently on A3 measured with the C detector is related to the passing minimum ionizing electrons. The spurious events would mostly be distributed around $A3_{P/b} = 0$ and a separation of this kind is indeed displayed by the results of Fig. 21. The spurious events in the data were eliminated by considering only those with A3>0.2 a.u..

The results on average waveforms for the PM1, PM2 and PM1+2 signals (Fig.23) are very similar, apart from amplitude, in contrast to that of the C detector which shows a different shape. This difference between the response of P/b and C can be ascribed to the contribution of the BC-444 scintillator in the former as previously noted in Fig.18b.

For the longitudinal response study, we used the measured A3 distributions of PM1, PM2 and PM1+2 which were analyzed with the help of a Gaussian-Landau function (cf. Fig.10). χ^2_{red} values of about 1 proved the goodness of the model. The Landau most probable value and the Gaussian standard deviation were used to obtain the mean value of the amplitude m, the resolution h besides the number of photoelectron (N_e). The results are presented in Table 10. The errors for μ were

estimated based on the statistics of the data giving typical uncertainties of about 1% which checks with the spread of the results for the repeated measurements at x = 0 mm. The μ variation is 47 and 14% for individual and summed PM tube signals, respectively. This improvement in the homogeneity of the detector response defines the benefit of the use of two PM tubes and the sum of their signals. We can also note that the μ values of the individual signals add up to those for PM1+2 within the errors. The results on η for the individual signals show a variation of 41% relative to an estimated error level of about 10%. The variation for the PM1+2 signal is much smaller (at the level of 8%). The relationship between the h values of PM1, PM2 and PM1+2 is not immediately discernible from the results in Table 10. Part of the variation in m and h can be ascribed to a dependence on position x as discussed below.

The results on the longitudinal response m(x) are presented for the PM1, PM2 and PM1+2 signals in Fig.24. The experimental points were fitted using double exponential functions of the form $y = a \cdot e^{-bx} + c \cdot e^{-bx}$ with the parameter values a=0.393/0.001/0.310, b=0.059/-1.094/-0.164, c=0.001/0.356/0.434, d=1.078/-0.059/0.119 for the three cases PM1/PM2/PM1+2.

The plots show that the amplitudes of the PM1 and PM2 signals have the same but mirrored longitudinal dependence, i.e., $\mu_1(-x) = \mu_2(x)$, with the errors of ±1 %. The amplitudes for the individual m(x) distributions were summed after renormalization, μ'(x), so that they take the same (average) value for x = 0, i.e., $\mu'_1(0) = \mu'_2(0)$. The thus created sum of reduced amplitudes, $\mu'_{1+2}(x) = \mu'_1(x) + \mu'_2(x)$, should represent the minimum x variation in amplitude measured with the P/b detector (Fig.24c). It is found that from a total amplitude variation of about 60 % over the full scintillator length of 90mm for the individual PM tube signals it can be reduced to about 15 % when the sum is used.

The observed variation in the resolution η(x) can be examined in terms of x' where x'=x for PM1 and x'=-x for PM2. The experimental results on η(x') for PM1, PM2, their average, PM1+2 besides the quadratic sum of η_1 and η_2 (SUM) are presented in Fig. 25. The experimental results for individual signals show a common trend. The η(x') curve features a variation from η = 24 to 38 % compared to η = 23 to 25 % for PM1+2. The η(x') curve for PM1+2 tends to indicate a peaking in the middle of the detector in contrast to the monotonic variation for the individual signals. For comparison with η_{1+2}, the resolution obtained by summing the individual values, i.e., EMBED Equation.3 is also shown in Fig. 25. This gives lower values than for η_{1+2} but may not exceed the uncertainties, especially, for the individual η values at x'=20 and 40 mm.

However, values η_{1+2} and η_{SUM} based on measurements with both PM tubes show a relatively small variation with x. The correlation of the A3 amplitudes of the individual PM tube signals is presented in Fig.26 as contour plot.

4.3 PROTON TESTS

Experiment 6 with the proton beam on the P/b detector was performed to mimic the detector operative condition at JET and study the waveform shape dependence on proton energy. The proton beam

energy band available was 1 to 7MeV in 1MeV steps plus one at 4.7MeV which proton range equals the thickness of layer L1. Results on averaged waveforms are presented in Fig.27.

The expected increase in amplitude with the beam energy (E_{Beam}) is evident as the change in shape for the transition region E_{Beam} = 4 to 5MeV. The latter is further demonstrated in the logarithmic plots of the results (Fig. 28). Here one can see that a drastic shape change happens between E_{Beam}= 5 and 6 MeV where the tail starting at t≈50 ns increases rapidly in amplitude with E_{Beam}, i.e., deeper proton penetration into L2. The early (t<10 ns) part of the waveforms shows some changes but with a less obvious relationship with E_{Beam} (Fig.27b and Fig.28b); this is further discussed in Sec. 4.4.

The A1-A2 scatter plot of the waveforms is shown in Fig. 29. For each energy, regions of high event density are formed whose centers follow an apparent linear variation with E_{Beam} (A1/A2=3.5) up to about 4.7 MeV (Fig. 29b) where A1≈2.1. Then only A2 increases with the proton energy. In other words, the A1-A2 plot illustrates the range measurement ability of the phoswich.

Some events occur near the origin of the plot and assemble along a line of approximately 6.5A1-A2≈0. These are interpreted to be due to noise as their amplitude ratio corresponds to that of the pulse height integration time, i.e., the gate ratio G1/G2. Moreover, the events of the low energy protons show distributions that are stretched in the same direction in contrast to those of higher energy. This suggests that the A1-A2 distribution pattern for 1MeV proton events is distorted by noise adding to the A2 values more than to those of A1. The A1-A2 representation of the results is also displayed in 3D plots (Fig.30). Here one can see that all distributions are rather symmetric around a central peak with the exception of the 1MeV distribution whose extra structure would be a manifestation of the noise effects.

The above results confirm that the chosen gates G1 and G2 work quite well for distinguishing protons in the energy range 1 to 7MeV. This was examined by splitting G1 into two, namely, G1a and G1b with the limits from -2 to 30ns and 30 to 60ns and analyzing the data in terms of the distributions A1a vs. A1b, and A1a and A1b vs. A2 (Figs.31a, b, c).

The results show that the A1a vs. A1b distribution has practically no E_{Beam} sensitivity in the range 5 to 7MeV, i.e., the protons that penetrate into L2. The distribution A1a vs. A2 is very similar to A1 vs. A2 (Fig.29a) but for the trivial difference that the A1a amplitudes are lower. However, this does not significantly affect the ability to separate events of different E_{Beam} which, indeed, is the case if the A1b-A2 representation is used. This shows that the definition of proton events with E_{Beam}>5MeV is not affected by the detailed choice of the G1 gate while the opposite is true for events due to E_{Beam}<5MeV. In other words, the A1 integration time affects the spread of proton events in the A1-A2 plots and this is to be minimized in order to enhance the ability to distinguish them from events generated by background. The investigation of the A1 resolution dependence on G1 was thus carried out and resulted in the optimal time interval [-2, 30] ns [24].

The amplitudes distributions A3, A1+2, A1, A1a, corresponding to decreasing integration time over the waveform data, were analyzed with Gaussian fits to determine the values of μ and η. The results are presented in Table 11 for each of the eight beam energies. The table also provides the

energy of the protons (E_p) at which they reach the scintillator taking into account the 6-mm aluminum foil wrapping [25]. Moreover, the relative amount of light that E_p protons produce in a homogenous scintillator is also given as derived from the $L(E_p)$ function presented in section 2. The systematic features of the energy dependence of the amplitudes are represented by $\mu(E_p)$ and $\eta(E_p)$.

The results on $m(E_p)$ for A3, A1+2 and A1a are presented Fig. 32 and compared with light yield curve $L(E_p)$. It is found that $m(E_p)$ follows $L(E_p)$ up to about 4.7MeV which is the limit for protons stopping in L1. This is most clearly displayed by the A1a amplitude which shows a sharp break in $\mu(E_p)$ at this point and a slight decrease with E_p beyond. The A1+2 amplitude shows the same E_p dependence up to 4.7 MeV where it starts to fall below $L(E_p)$ due to the difference in light yield between L1 and L2.

The results on the resolution as function of energy, $\eta(E_p)$, are compared with the projected variation based on $\eta_L(E_p)=L(E_p)^{-1/2}$ (Fig.33). The results for A1a show approximately the projected E_p dependence while those for A1+2 and A3 differ at $E_p = 0.7$ and 1.8MeV due to the interference of noise. This can be estimated for A1a, A1, A3 at $E_p = 0.7$MeV from the combined use of m and h in Table 11 assuming the relationship $\eta \approx k/\sqrt{\mu}$ with the proportionality factor k derived by the A1a result. The estimated noise contribution is assumed to be 3% per 10ns and through the integration times of 30, 60 and 420ns one would account for the measured h values in the table and also estimate similar intrinsic signal resolution values for A1a, A1, and A3, namely, η=36, 39 and 31%, respectively. The noise effect on the value for A1a is small as compared to the measured value of 37% in contrast to the situation for A1+2 and A3 where h is estimated to be inflated by noise for $E_p \leq 1.8$MeV as borne out by the results in Fig.33. Considering the noise effect, the measured resolution values show the expected variation and the remaining scatter would be within uncertainties of the statistics of the data. It can be noted that the E_p dependence of the h values shows a kink at about 4.7 MeV reflecting the saturation of the energy deposition in L1 while that in L2 gives less light. The light yield in L2 is only reduced by a factor of 1.7 due to its optical properties lowering the resolution by less than 25 % for the two highest E_p points which is at the level of errors.

4.4 COMBINED TESTS WITH ALPHAS AND BETAS

The P/b detector was studied in experiment 7 with radiation from the a and b sources with enhanced statistics so as to detect and utilize weak features in the data. In this test the full [106]Ru source emission, namely β's and γ's, is considered as it provides background components similar to the ones expected in the application at JET. This is different from test 5 where accidentals were removed from the data.

The features of interest in this experiment are those related to events due to different (high and low) energy depositions with a's and b's in the fast (BC-404) layer of the phoswich. Due to the source configuration, some a's feature longer paths to the scintillator so the 5.5-MeV main component would have also a weak low energy tail. The'b source emits a continuous spectrum up to 3.5 MeV but only a small fraction deposit energy only in the L1 layer because of the relative long range.

Therefore, special care had to be taken in identifying the high and low energy deposition events involving L1 only, as described in detail below. Moreover, high and low energy deposition events were also recorded using the M2 detector, under the same experimental conditions as for the P/b, in order to assess the effect of BC-444 on the response of BC-404 in the phoswich.

The results in terms of A1 vs. A2 distributions for a on P/b are presented in Fig.34a. Here one can see that the a distribution has a high density region centered at A1/A2=2.1/0.3 corresponding to α's impinging on BC-404 with the full 5.5MeV energy; the deposited energy would correspond to 0.4MeV electrons (0.4MeVee). There is also a low-density tail which can be ascribed to low energy'a's extending towards the origin but with a cut-off at A1 = 0.5 due to a pulse height threshold in the electronics. One can also see an apparent boundary for the event distribution approximately described by A1-2.7A2≥0.

The results for β's (Fig.34b) show an event distribution that extends'beyond the region of the α's, especially, with regard to high A2 amplitudes. This reflects the fact that the electrons can deposit energy up to 3.5MeV involving both scintillator layers compared to the α's maximum of 0.4MeVee in BC-404. This means that the β's can deposit as much or more energy than the α's without exiting the L2 layer. The β's, which do not deposit energy in L2, produce events with a distribution similar to that of the a's, i.e., a ridge along line A1-7A2 = 0 in Fig.34b. The β's depositing energies below 0.15MeV correspond to A1 = 0.8 a.u. and produce a distribution reflecting the source spectrum which, however, is truncated by the cut-off at A1≈0.5.The deposited energy can exceed 0.15MeV if the β's impinge non-perpendicularly on the scintillator surface and/or if they backscatter in the L1 layer. It can be noted that most β's interact in both scintillator layers of the P/β detector producing events whose A1/A2 amplitude ratio reflects the product of thickness (0.3:2.5) and light yield (1.0:0.6) ratios of the scintillators, i.e., A1/A2 ≈ 1/5. Depending on the angle of incidence, these passing β's would be distributed in the general direction 5A1-A2>0.The data recorded with the α and β sources were superimposed and the resulting A1-A2 event distribution is represented with contours of equivalent event density (Fig.35). Here one can see the region of maximum density due to 5.5MeV α's centered at (A1, A2) = (2.1,0.3) as identified in Fig.34. Moreover there is a weaker maximum centered at (A1, A2) = (0.8, 0.11). Both of these maxima lie on the line A1-7A2 = 0 that correspond to radiation interacting with the BC-404 scintillator only. Hence, events in two distinct regions were selected, namely, the high and low energy boxes 1.8/0.25 ≤ A1/A2 ≤ 2.3/0.4 and 0.7/0.05 ≤ A1/A2 ≤ 1.2/0.25 shown in Fig.35. The α and β events falling in the boxed regions were used to study waveforms in BC-404 depending on type of particles and difference in deposited energy.

The results on the average waveforms for α's and β's of high and low deposited energies are shown in Fig. 36 where the average waveforms are normalized with respect to the peak. As one can see the waveforms are very similar with a detailed difference in the falling edge of the pulse (time interval t = 8 to 50ns). The waveform for high energy is slightly higher in this interval for both α's and β's while the difference between them for given energy deposition is vanishing small. One can also make the comparison based on peak widths where the waveforms differ by about 2ns (FWHM) between

14

high and low energies and less than 1ns between α's and β's. Thus, there is a difference between the high/low cases for both a's and b's but very small dependence on type of radiation. The response of the P/b detector to b radiation was compared to that of the monolithic BC-404 scintillator of the M2 detector (test 7b) in the same high/low energy regions. The results on the average waveforms of events selected in this way are presented in Fig.37 normalized as in Fig.36. It is found that the waveform shape for the M2 detector shows no difference for both low or high-energy deposition compared to that observed for detector P/b.

The difference in P/b response for high/low energy events is localized from the maximum of the waveform over the interval up to t≈40 ns. In fact, detector M2 produces waveforms of much steeper falling edge and similarly narrower width, i.e., 13 ns (FWHM) compared to 16 and 18 ns for P/b. This might be due to particle range and solid angle effects within the phoswich detector (cf. Figs. 27b and 28b for protons in test 6).

The comparison is also made between the response of detectors P/b and M1 obtained in test 3 as presented explicitly in Fig. 38 where the average waveforms are normalized with respect the amplitudes A1. Here it is interesting to note that the detector response is not very sensitive to the light transport path in the scintillators. An explanation for such different behavior of the monolithic and phoswich detectors can be found looking at the distribution of light emission wavelength: Some of the light produced in BC-404 can be absorbed by BC-444 and promptly re-emitted. In other words, the latter process effectively acts as a waveform converter so that the BC-404 pulse in a monolithic scintillator corresponds to one for the phoswich that is an intermediate between that of BC-404 and BC-444.

DISCUSSION

The pulse shapes of the phoswich detector events are used to provide information on the range of incoming radiation to identify and separate proton events from background signal. In the present application, the desired events are due to protons impinging on the L1 side of the phoswich while background radiation of Compton electrons, γ's and neutrons can come from any direction: Electrons are generated by γ's while neutrons can produce proton recoils in the scintillator. The range information obtained on the proton signals enhances the identification beyond what the pulse height can provide.

As the phoswich will be used in the focal plane detector of the MPRu, the proton energy is limited to the energy ranges of neutrons from the $d + d \rightarrow {}^{3}He + n$ and $d + t \rightarrow a + n$ reactions centered around 2.5 and 14MeV, respectively. As the momentum of protons impinging on each scintillators is well known, the resolution of the measurement depends only on the pulse height distribution of the proton signals. The amplitude and resolution varies depending on the layer of the phoswich in which the energy is deposited as shown in Table 12. Information is extracted from the tests with different types of radiations and related to the recoil protons for dd and dt fusion neutron measurements. Table 12 contains six different cases:

1. Minimum ionizing electrons passing through detector perpendicularly.
2. 5.5MeV a's stopping in layer L1.
3. 2.5MeV protons from dd neutrons stopping in L1.
4. 3MeV protons from accelerator beam (test near to the 2.5MeV case).
5. 5MeV protons with range corresponding to the L1 thickness.
6. 14MeV protons from dt neutrons passing through L1 and stopping in L2.

Test results exist for cases 1, 2, 4 and 5 while cases 3 and 6 represent the measurement situations when the detector will be used in the MPRu set to record 2.5MeV dd and 14MeV dt neutrons. The table gives information on the actual deposited energy for the different cases in layers L1 and L2, respectively, and the total deposited energy (L1+L2); for electrons only the latter quantity is measured in the tests. With the help of the information in Fig.2 the deposited energies for the radiation of interest have been expressed in equivalent electron energy (MeVee). The last column gives the light yield relative to 5.5MeV α's considering also the different light output characteristics of L1 and L2 [19, 23].In order to improve the pulse height definition of the proton signals, the MPRu phoswich elements are equipped with two PM tubes attached to each scintillator and the summed signal is used. This reduces the position dependence of the scintillators response from more than 50% over the 90mm length of the prototype P/b detector to 15% from center to either end (Fig.24). This position dependent variation in pulse height response affects the measurement resolution and can be estimated to correspond to a Gaussian width of about 8% (FWHM). This is a limited contribution to the pulse height resolution of proton signals of given energy which is predominantly determined by the photoelectron statistics. The latter, for instance, is estimated to be 16% (FWHM) as measured for the A1 distribution for E_{Beam} = 3MeV (Table 11). (It can be noted that this is consistent with the value of 22% obtained for E_α = 5.5 MeV of Table 7 at relative light yield of 1 compared to about 2.5 for E_{Beam} = 3MeV). The effect of the position dependent pulse response of summing the two PM tube pulses would give a total resolution of about 14% instead of 11%. It is important to note that the summation of the two PM tube signals can be done if the pulse shape does not change with position which was confirmed by the test 3 with α's (Fig.38).

The noise also plays a role in pulse height measurement. The signal/noise ratio is important for the measured waveforms in terms of pulse height as function of time, P(t). It is found in the present study that the observed pulse height resolution is affected by noise for protons of E_p< 3MeV and increases with integration time; it is smallest for the A1 distribution and larger for those of A2 and A3. The tests have demonstrated that the pulse shape changes depending on energy deposition in the layers L1 and L2 of the phoswich. The waveforms were integrated over the peak and tail regions to determine the amplitudes A1 and A2 as a trade off between need to reduce the statistical variation and keep sensitivity to shape changes for individual waveforms. With the a's of short range, it was thus shown in test 1 that the difference in the event distributions in A1-A2 plots depends on energy deposition in either L1 or L2. With protons of variable energy illuminating the L1 layer (test 6), it was shown that the events are localized along a linear ridge for E_{Beam} up to 4.7MeV and follow

16

another ridge of nearly constant A1 value for high E_{Beam} when the protons pass through L1 and enter L2. This illustrates that events at a constant value of A1 can be identified as protons with the A2 value reflecting their total energy. Electrons represent yet another case as they appear as minimum ionizing radiation already at low energy (1MeV) and pass through both layers depositing 0.06 and 0.5 MeV respectively (test 5).

The detailed waveform response of the phoswich detectors was studied based on the average of the summed event pulses to get the typical shape for test measurement of interest. This is important as one wants to know to which degree the phoswich responds with a waveform shape whose topology is given by the relative amount of light produced in the L1 and L2 layers and/or if other factors play a role such pulse magnitude and type of radiation. This was the objective of a special study (test 7) where events recorded in L1 due to α's of high (5.5MeV) and low energy were selected and compared with b events in the same energy regions. A shape difference could be detected in the results where the high-energy events gave a 15% higher pulse height at t = 20ns for both α and β radiation (Fig.36). This can also be expressed as an increase in width from 16 to 18ns (FWHM). However, changes in the waveforms at this time scale have no practical influence on the pulse shape analysis undertaken to identify, say, protons of varying penetration depth (Fig.39). For comparison, the waveforms of minimum ionizing electrons are also shown which tail appears to be similar to that of 7MeV protons. On closer inspection (Fig.39b) one can see that there is a distinct difference in their widths, namely, 13 ns compared to 19 and 27ns for 2 and 7MeV protons, respectively. The greater width is an effect of the different setup, i.e., cable length, and light emission in the detector. The light output of 2 and 7MeV protons is about a factor 1.7 and 4.9 larger than that due to $β_{min}$'s in the phoswich detector.

In the experiment at JET, the detector would be distant from the data acquisition system by about 120m which was measured in this study (test 4) to increase the waveform width to about 30ns (Table 9). This would have no detrimental effect for pulse shape analysis based on the A1-A2 representation with the gates used. The negative effect would mostly refer to the sensitivity to noise for low proton energy.

Based on the test studies presented here and other results, the focal plane hodoscope with phoswich detectors (cf. Table 4) has been built and mounted in the MPRu spectrometer. The spectrometer has been used in experiments since 2006 mostly in measurement of 2.5MeV dd neutrons. The detector works as envisaged which means that the 2.5MeV protons can now be clearly separated from the background based on the information provided by the phoswich scintillators.

This is illustrated in Fig.40a where the distribution due to 2.5MeV proton events in a central phoswich scintillator is well localized in the A1-A2 plot, and quite separated from the bulk of background events. The background events appear within the region of lower A1 and A2 values and only the tail of their distribution is stretched, exponentially decreasing, towards the proton region as presented in Fig.40b. The background events are caused by electron, g and neutron interactions in the phoswich detector element. By selecting events in the proton region the S/B ratio can be further

improved through specific waveform comparison. These distributions measured at JET reflect the ones obtained in test 7 (Fig.34b) and in test 6 with the accelerator beam (Fig.40c). The resolution of the distribution A1 of the 2.5MeV protons is about 25% (FWHM) [26].

CONCLUSIONS

This paper has reported on a series of tests of phoswich scintillation detectors for installation in the magnetic proton recoil spectrometer as part of MPRu upgrade project at JET. The objective of the study was to perform laboratory testing of prototypes to verify the technique to achieve significantly better ability to handle the interference of background in the JET measurements over the entire energy range of fusion neutrons, i.e., 1.5 to 18MeV than that obtained with the MPR hodoscope of monolithic scintillators. Specifically, this entailed making the signals of protons from $d + d \rightarrow {}^{3}He + n$ reactions more distinct by choosing a phoswich scintillator where the first layer has a thickness matching the range of protons of $E_p < 5$MeV (i.e., 0.3mm) while the full thickness matches the range for $E_p < 18$MeV (about 3mm). Protons are separated from background based on amplitude and shape of the generated pulses; the precision for this separation is essential for the ability to distinguish desired proton signals from undesired background radiation. To investigate this, the prototypes were tested with α and β radiation from radioactive sources and with protons from an accelerator beam. The tests consisted of measuring the detailed waveforms of the radiation-generated pulses and to determine to what extent integration over two or more time periods (for instance, amplitudes A1 and A2) would be sufficient to identify the radiation and which factors would affect the efficiency of this data reduction method. It was found that elongated phoswich scintillators ($90 \times 10 \times 3$ mm^{3}) with a PM tube at each end and summing their signals can be used to measure protons over the energy range 1.5 to 18 MeV. A standard short (A1)-long (A2) gate analysis of the acquired pulse shapes provided well-localized proton "islands" in the A1-A2 distribution plot with sufficient separation of signals from background, which generally is spread out over a much wider area in the A1-A2 parameter space.

A central factor for good identification of protons is the attainable pulse height resolution. An important aspect in this context is the variation in pulse height depending on the longitudinal position of the event in the scintillator. It was found that the position-dependent pulse height variation had a small effect on the pulse height resolution for the summed output from the two PM tubes. However a significant gain in light collection efficiency (about a factor 2) was observed when a backing of plastic (light guide material) was added: Specifically, based on the proton tests, the pulse height resolution (FWHM) in the range 2-3MeV was found to be 28%-16% (A1). Thus, pulse height resolution was deemed to be adequate for protons of energies of the intended application but it was noted that noise interference could be a degrading factor. This will, partly, be due to the need of use of rather long cables (120m) whose effect on the pulse shape event identification was tested with respect to signal dispersion; it was found that the increased pulse width caused by the cable of a hundred meter length would not significantly alter the typical A1/A2 pattern for protons, but only have an effect increasing the sensitivity to noise in the event separation process.

Finally, the results of the tests have provided the basis for the construction design of the phoswich hodoscope installed on MPRu. Preliminary results from 2.5MeV dd neutron measurement demonstrate that the MPRu works in line with projections made from the tests described in this study. Especially, MPRu neutron spectrometer represents a hundred-fold increase in signal to background ratio over the original MPR thereby validating the results of simulation calculation [27]. The resolution of the measured proton distribution is found to be 25%. This shows that the MPR is suitable for neutron emission spectroscopy diagnosis of D plasmas. It also puts confidence in the simulation results for the measurement of the 14MeV neutron emission in DT plasmas, where substantially background free measurements are predicted ($S/B \approx 2\times10^4$).

ACKNOWLEDGMENTS

REFERENCES

[1]   O.N.Jarvis, Nucl. Instr. Meth. A **476** (2002) 474.

[2]   J.Källne and G.Gorini, 'Proceedings of the International Course and workshop on diagnostics for contemporary fusion experiments', (Varenna, August 1991), Società Italiana di Fisica, Bologna, ISBN 88-7794-043-3, 1033.

[3]   J.Källne and G.Leman, Uppsala University Neutron Physics Report, UU-INF #93/1 (February 1993) unpublished.

[4]   J.Källne et al., Rev. Sci. Instr. **70** (1999) 1181.

[5]   M.Tardocchi et al., Rev. Sci. Instr. **72** (2001) 836.

[6]   H.Henriksson, "Neutron spectroscopy studies of heating effects in fusion plasmas", PhD Thesis Uppsala University, Uppsala, Sweden, (2003) unpublished.

[7]   J.Källne et al., Physical Review Letters **85** (2000) 1246.

[8]   H.Henriksson et al., Plasma Physics and Control. Fusion **47** (2005) 1763.

[9]   L.Giacomelli, 31st EPS Conference on Plasma Phys. London, 28 June - 2 July 2004 ECA Vol.28G, P-5.171 (2004).

[10] J.Källne and H.Enge, Nucl. Instr. Meth. A **311** (1992) 595.

[11] J.Frenje, "Instrumentation for fusion neutron measurements and experimentation at JET.", Uppsala : Acta Universitatis Upsaliensis, 1998.- viii, 70s. (Comprehensive summaries of Uppsala dissertations from the Faculty of Science and Technology, ISSN:1104-232X; 335).

[12] A.Hjalmarsson, "Study of signal to background ratio in fusion neutron spectroscopy measurements at JET for next step tokamak applications", Uppsala Univ. Neutron Physics Report (September 1999) unpublished.

[13] J.Källne, "The JET Enhancement project: The Magnetic Proton Recoil Upgrade (MPRu) as a Neutron Spectrometer Diagnostic". The EFDA JET/CSU Project summary (2002).

[14] G.Ericsson et al., *Proceedings of the Workshop on Diagnostics for ITER*, Varenna, Italy, September 2001 (Plenum, New York, 2001), p. 121.

[15] A.Combo et al., Fusion Eng. and Design, **71** (2004) 151.

[16] HYPERLINK "http://www.bicron.com" http://www.bicron.com.

[17] HYPERLINK "http://ie.lbl.gov/toi/nuclide.asp?iZA=450106" http://ie.lbl.gov/toi/nuclide.asp?iZA=450106.

[18] L.Giacomelli, "Development of instrumentation for neutron emission spectroscopy diagnosis of fusion plasmas in deuterium", Diploma Thesis Uppsala University, Uppsala, Sweden, (2002) unpublished.

[19] G.F.Knoll, "Radiation detection and measurement" (New York: John Wiley&Sons, Inc.), 1999, p.32.

[20] T.J.Gooding and H.G.Pugh, Nucl. Instr. Meth. **7** (1960) 189.

[21] http://www2.tek.com.

[22] S.Marrone et al., Nucl. Instr. Meth. A **490** (2002) 299.

[23] G.F.Knoll, "Radiation detection and measurement" (New York: John Wiley&Sons, Inc.), 1999, p. 90.

[24] L.Giacomelli, private documentation.

[25] HYPERLINK "http://physics.nist.gov/PhysRefData/Star/Text/PSTAR.html" http://physics.nist.gov/PhysRefData/Star/Text/PSTAR.html.

[26] H.Sjöstrand et al., Rev. Sci. Instr. **77** (2006) 10E717.

[27] G.Wikström, "Performance studies of phoswich detectors in the upgraded Magnetic Proton Recoil neutron spectrometer", UU-NF 05/#01, Uppsala University, Neutron Physics Report ISSN 1401-6269 (February 2005) unpublished.

FOOTNOTES

1 *These amplitudes represent the amount of charge collected at the anode of the PM tube during the pulse evolution.*

2 *The fluctuations can be due to statistics or noise as we shall discuss later.*

3 *Note that the notation $\mu'_{1+2}(x)$ stands for summation of the renormalized individual amplitudes in contrast with $\mu_{1+2}(x)$ for PM1+2 in Table 10.*

4 *The light yield L corresponding to E_p has been calculated using a power fit of the proton light output presented in Fig.2 [20], namely, with $L = a \cdot E_p^b E_p$ in MeV, a= 0.0017 and b=1.3409. The goodness of the fit has been verified through the R^2 parameter that equals 0.9996 and the results are included in Table 11. These results are graphically represented as a function of E_p in Figs.32 and 33.*

5 *Of which only a fraction is likely to be deposited because of the long range of such electrons compared to the scintillator dimensions.*

6 *This comes from the information that 5.5-MeV α's appear with A1=2.1 corresponding to an equivalent electron energy of 0.4 MeVee.*

7 *With the above information one can determine that the response of detector P/b in terms of the A1/A2 ratio is 7:1 for L1 and 1:5 for L1+L2 approximately.*

	BC-404	BC-444
Rise Time, ns	0.7	19.5
Decay Time, ns	1.8	179.7
Wavelength of Max. Emission, nm	408	428
Light Output rel. to Anthracene (%)	68	41
Index of refraction	1.58	1.58
Bulk Light Attenuation Length, cm	160	180
No. of H Atoms per cm^3, ($\times 10^{22}$)	5.21	5.25
No. of C Atoms per cm^3, ($\times 10^{22}$)	4.74	4.73
Ratio H:C Atoms	1.100	1.109
No. of Electrons per cm^3, ($\times 10^{23}$)	3.37	3.37

Table 1. Optical and composition properties of Bicron BC-404 and BC-444 plastic scintillators.

	BC-404 and -444	BC-800
Base	Polyvinyl toluene	Decolorized methyl methacrylate monomer
Density	1.032 g/cm^3	1.19 g/ cm^3
Refractive Index	1.58	1.49
Coefficient of Linear Expansion	7.8×10^{-5}, below 65°C	7.4×10^{-5}/^{o}C
Softening point	70°C	96°C
Vapor Pressure	Vacuum compatible	Vacuum compatible

Table 2. Physical properties of Bicron BC-404 and BC-444 plastic scintillatorsand BC-800 acrylic plastic.

Detector type	Thickness [mm]			Length [mm]	Width [mm]
	BC-404	**BC-444**	**BC-800**		
P	0.3	2.5	0	90	10
P/b	0.3	2.5	5	90	10
M1	3.5	0	0	100	20
M2	2.8	0	0	100	8
C	2.8	0	0	8	8

Table 3. Summary of the sciatillator dimensions of tested detectors.

Detector type	Thickness [mm]			Length [mm]	Width [mm]
	BC-404	**BC-444**	**BC-800**		
III	0.3	2.2	1.3	100	20
IV	0.3	2.5	5	100	10
V	0.3	2.5	5	100	10
VI	0.3	3.2	0	100	20

Table 4. Summary of scintillators dimensions of the MPRu detectors. Type IV and V were placed at the center of the hodoscope, type III and VI on the low and high-energy sides.

Test		Scintillator	Light guide	PM tube	
#	**Source**			**Type**	**#**
1	α	P	Fishtail	H	2
2	α	P/b	Cylindrical	H	2
3a	α[1]	P/b	Cylindrical	H	1
3b	α[1]	M1	Fishtail	E	1
4	α	P/b	Cylindrical	H	1
5	β_{min}[2]	P/b	Cylindrical	H	2
6	p	P/b	Cylindrical	H	1
7a	α, β[3]	P/b	Cylindrical	E	1
7b	β[3]	M2	Fishtail	E	1

[1] *Source moved along the scintillator.* [2] *β_{min} source and C detector mounted on xy-table.*
[3] *The emission from the uncollimated ^{106}Rh source.*

Table 5. List of tests and detectors used as combinations of scintillator, light guides and PM tubes (type and number).

E$_{Beam}$ (MeV)	Nominal (MeV)	Effective (MeV)	Waveforms	Trigger level (MV)	Average pulse height
1	0.990	0.982 ± 0.001	2000	-17	-20
2	1.990	1.973 ± 0.002	4000	-30	-55
3	2.990	2.964 ± 0.003	4000	-30	-100
4	3.990	3.953 ± 0.004	4000	-30	-134
4.7	4.700	4.654 ± 0.005	4000	-30	-151
5	4.990	4.941 ± 0.005	4000	-30	-150
6	5.996	5.934 ± 0.006	3500	-30	-142
7	6.988	6.912 ± 0.007	3500	-30	-133

Table 6. Summary of nominal and effective proton beam energies used and data acquisition information of number of waveforms recorded, trigger threshold settings compared to average pulse height generated.

Test	Amplitude	Waveforms	PM1			PM2				PM1+2		
			μ	η [%]	N$_e$	Pulse height [mV]	μ	η [%]	N$_e$	μ	η [%]	N$_e$
L1(P)	A1									0.36	32	53
	A2									0.04	157	2
	A3	4000	0.21	48	24		0.19	45	27	0.40	36	43
L2(P) [1]	A1									0.08	68	12
	A2									0.14	68	12
	A3	2823	0.12	72	11	72	0.12	69	12	0.24	59	16
L1(P/b)	A1									0.89	22	118
	A2									0.09	119	4
	A3	4000	0.50	33	52	70	0.49	31	58	0.99	25	90

[1] Only events with A3>0.03 a.u. were selected.

Table 7. Summary of results on amplitude distributions A1, A2 and A3 for α's interacting in L1 and L2 of detector P and L1 of P/b with extracted information on mean pulse amplitude (m) in [a.u.], pulse height resolution (h) and derive photoelectron statistics (N$_e$)for PM1, PM2 and PM1+2.

A3	η_1	η_1	η_{1+2}	η_{SUM}	ρ
L1(P)	48	45	36	33	0.19
L2(P)	72	69	59	50	0.41
L1(P/b)	33	31	25	22	0.25

Table 8. Results on pulse height resolution for α's recorded in L1(P), L2(P) and L1(P/b) for signal from PM1, PM2 and PM1+2 (η_1, η_2 and η_{1+2} in percent) besides η_{SUM} derived as the quadric sum of η_1 and η_2 (see text). Results on the correlation coefficient ρ are also shown.

L_C (m)	Relative peak value	Rise time (ns)	FWHM (ns)
0	1	4	10
4	1	6	10
53	0.5	6	18
121	0.3	8	30

Table 9. Relative peak value, rise time and width of the average waveforms due to α's onto L1 of P/b recorded by PM1 tube in test 4 with RG-58 cables of different lengths L.

Position	Waveforms	PM1				PM2				PM1+2		
x		$A3_{th}$	μ	η	N_e	$A3_{th}$	μ	η	N_e	μ	η	N_e
(mm)		(a.u.)	(a.u.)	(%)		(a.u.)	(a.u.)	(%)		(a.u.)	(%)	
0	1347	0.2	0.39	33	52	0.2	0.35	35	44	0.73	26	83
-20	1327	0.2	0.45	30	63	0.2	0.32	37	41	0.77	24	99
-40	507	0.3	0.57	23	105	0.15	0.28	41	32	0.86	23	103
0	1287	0.2	0.39	30	61	0.2	0.36	34	48	0.75	25	92
20	1250	0.2	0.35	31	57	0.2	0.41	28	69	0.77	25	90
40	603	0.15	0.31	34	47	0.3	0.53	24	99	0.87	25	91
0	1341	0.2	0.40	33	51	0.2	0.36	32	54	0.76	24	93
0 (sum)	3975		0.39	32	55		0.36	34	49	0.75	25	89

Table 10: Summary of the results on the A3 amplitude distributions for β_{min} radiation illuminating the P/b detector at different longitudinal position. Information is given on the source position relative to center x=0mm, A3 thresholds used, number of waveforms analyzed besides derived results on amplitude mean value (m), resolution (h) and number of photoelectrons (N_e) for PM1, PM2 and PM1+2.

E_{Beam} (MeV)	E_p (MeV)	L (10^{-2})	μ (a.u.)				η (a.u.)			
			A3	A1+2	A1	A1a		A1+2	A1	A1a
1	0.7	0.1	0.25	0.24	0.19	0.17	129.8	98.9	43.0	37.2
2	1.8	0.4	0.82	0.81	0.64	0.52	49.1	36.1	27.5	27.1
3	2.9	0.7	1.54	1.53	1.21	0.97	26.3	20.1	16.3	16.0
4	3.9	1.0	2.24	2.21	1.72	1.34	21.1	16.8	14.1	13.3
4.7	4.6	1.3	2.72	2.67	2.03	1.56	16.3	13.2	10.9	10.4
5	4.9	1.4	2.75	2.69	2.00	1.54	16.4	13.4	11.0	10.2
6	5.9	1.8	3.57	3.39	2.03	1.50	15.6	12.6	11.6	11.4
7	6.9	2.2	4.25	3.94	2.03	1.47	16.2	13.0	12.7	12.6

Table 11: Summary of the results on amplitude mean value m and resolution h for the A3, A1+2, A1 and A1a amplitude distributions generated by protons of different energies impinging on the P/b detector.

Layer	Case		MeVα	MeVp	MeVee	L[1]
L1	1	0.06				0.2
	2		5.5	(1.6)	0.4	1.0
	3			2.5	0.8	2.0
	4			3	1.0	2.5
	5			5	2.0	5.0
	6			1.1	0.3	0.7
L2	1	0.5			0.5	0.7
	6			12.9	7.0	10.5
L1+L2	1	0.56[2]				0.9
	6			14	7.3	11.2

[1] Relative light yield normalized to $L_\alpha = 1$ for $E_\alpha = 5.5$ MeV deposited in L1.
[2] Deposited energy for minimum ionizing electrons passing perpendicularly through the phoswich detector P/b.

Table 12: Summary of calculated energy deposition of electrons, protons and a particles in layers L1 and L2 of the phoswich detector for different irradiation cases relating to the tests performed (1, 2, 4 and 5) and envisioned measurements of recoil proton of 2.5 and 14MeV neutrons (3 and 6). The deposited energies are also expressed in terms of equivalent electron energy (MeVee) and relative light yield where the difference of a factor 0.6 between L1 and L2 is included.Layer
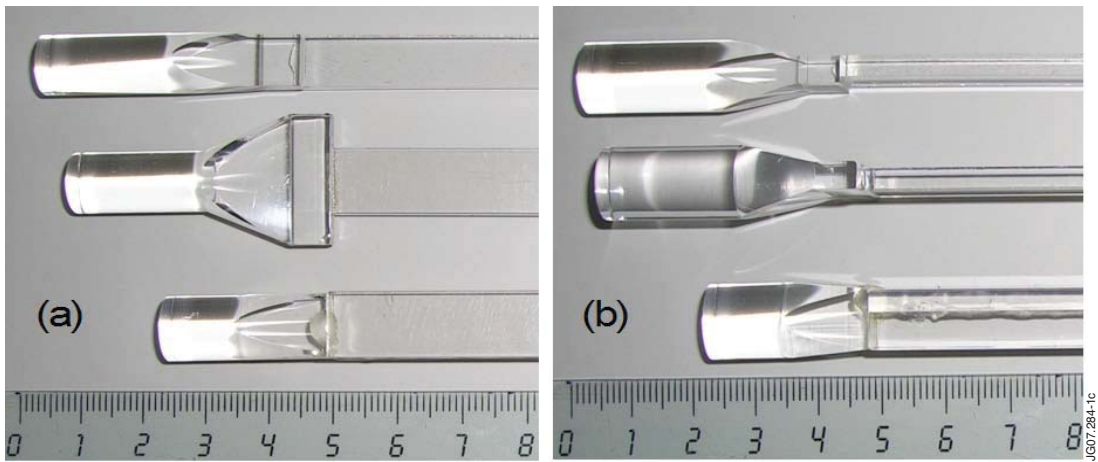
Figure 1:a Photos of fishtail and cylindrical light guides attached to detectors M2, P and P/b, from top; front (a) and side (b) view. The scale is shown in centimeters.
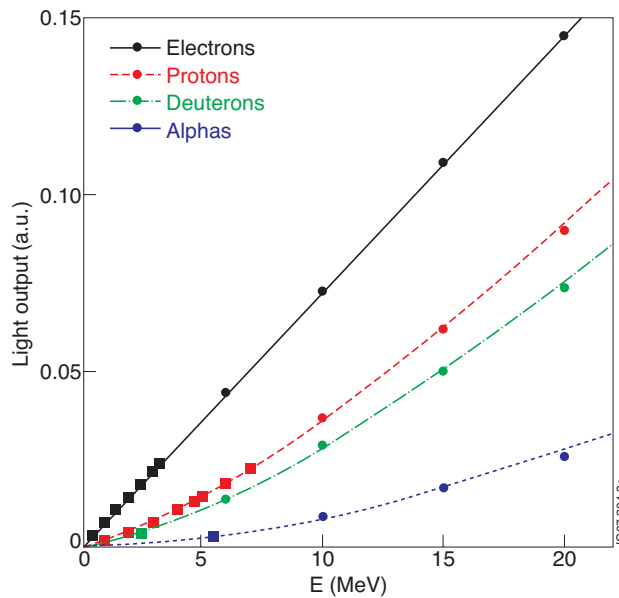
Figure 2: Light output as a function of the deposited energy for different particles stopping in plastic scintillator NE 102, BC-400 equivalent. Adapted from [20]. The squares in the plot indicate the radiation energies of interest for the tests.
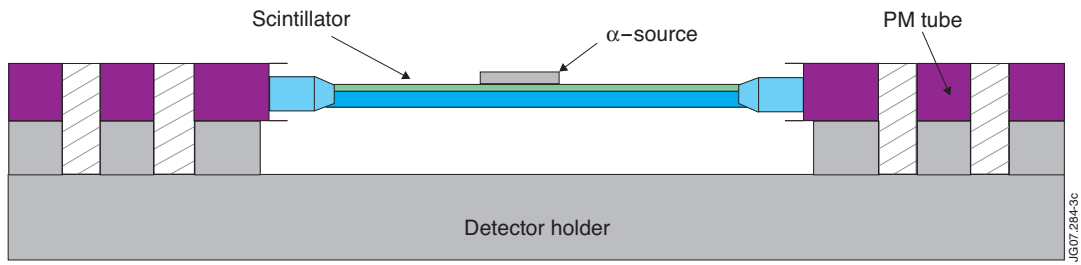
Figure 3: Sketch of the setup used for the a tests 1, 2 and 4.
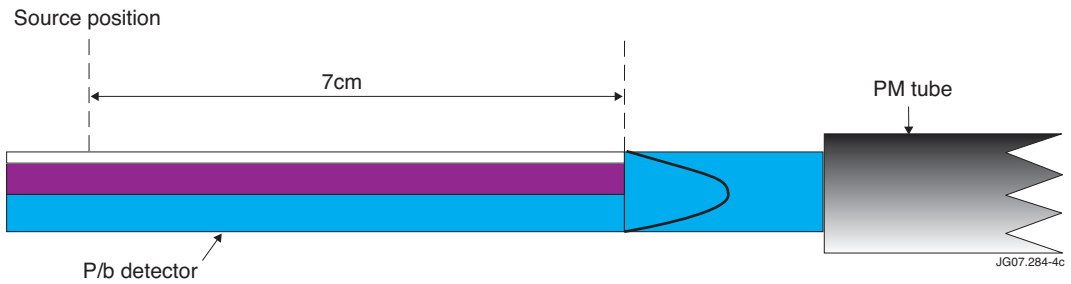
Figure 4: The setup used for a test 3 and a and b test 7.
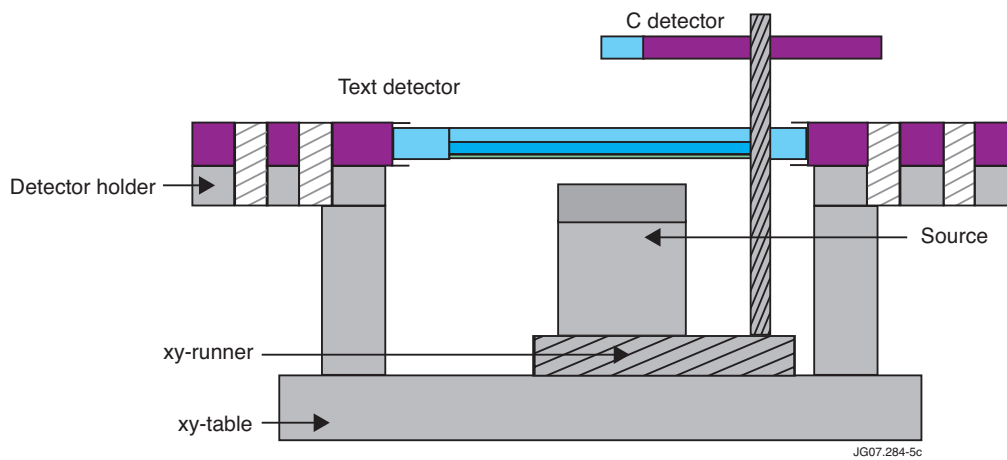
Figure 5: Sketch of the setup used for the longitudinal b mapping of the detector P/b (test 5). The β source is placed below a lead cap collimator (2-mm diameter) fixed on the xy-table.
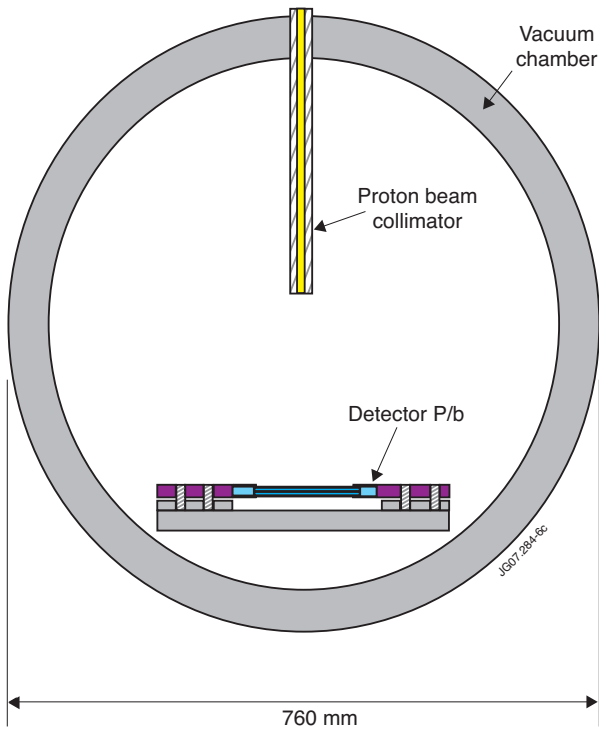
Figure 6: Sketch of the setup for test 6 with a beam of protons from Uppsala Tandem Accelerator with the test detector placed in a vacuum chamber at 2×10^{-6} mbar. The beam was defined with a 5-mm diameter collimator at a distance of 300mm from the scintillator.
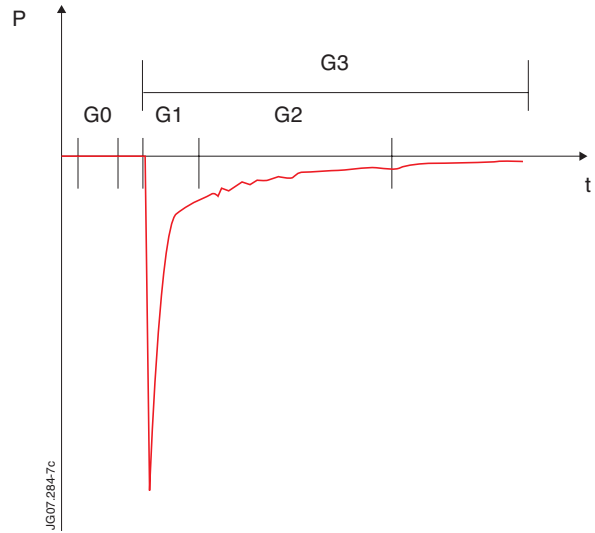
Figure 7: Schematics of the waveforms (pulse height as function of time) generated by ionizing radiation in the phoswich scintillators and the time gates (G0, G1-3) used to define the time-integrated information on the pulse (referred to as amplitudes).
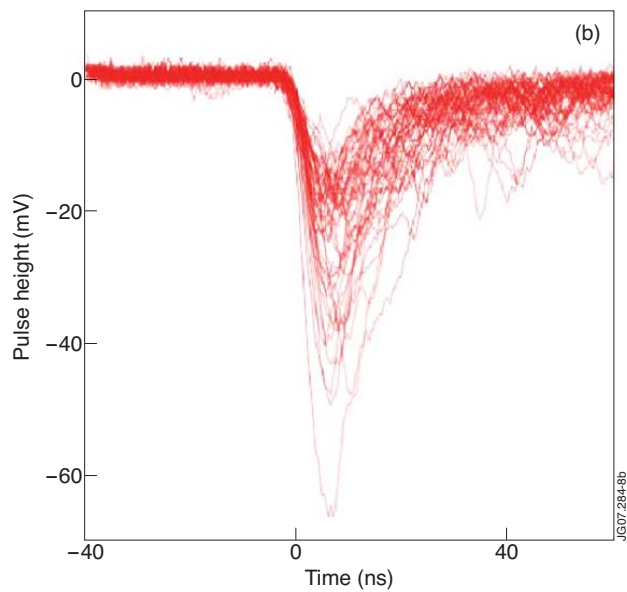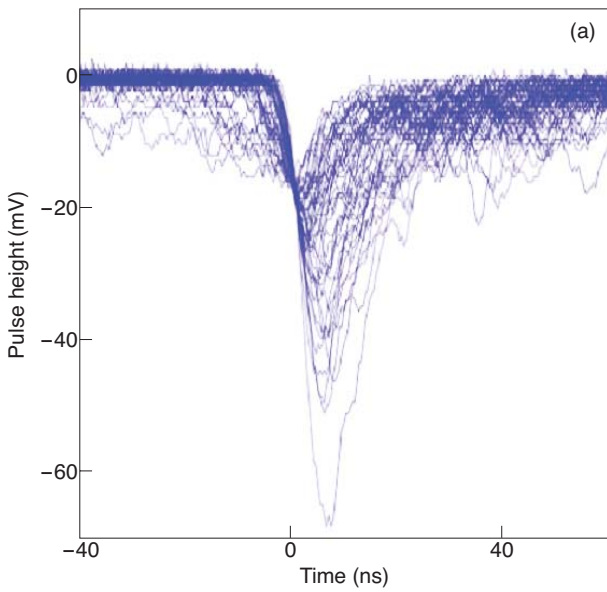
Figure 8: Examples of β waveforms from ^{106}Ru source recorded in test 7 with a fixed trigger threshold, (a), and after the constant fraction reduction at 25% of pulse height maximum for each event, (b).
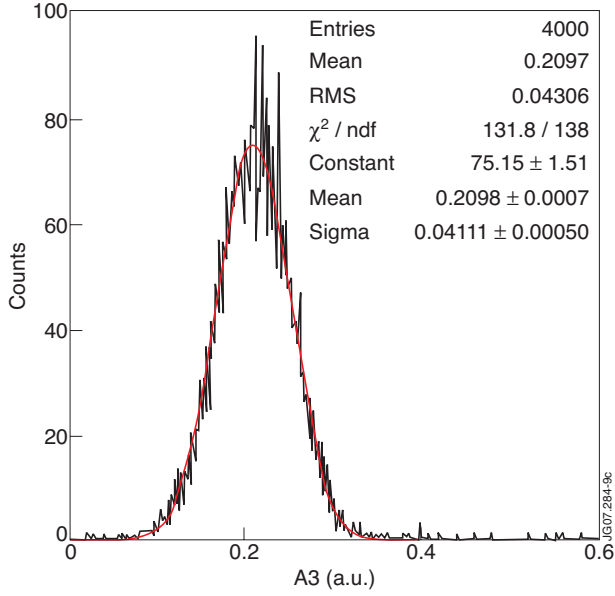
Figure 9: Example of measured amplitude distribution (A3) with PM1 tube in test 1 with the a's stopping in layer L1 (BC-404) of detector P at the mid point; the Gaussian fit is shown in red.
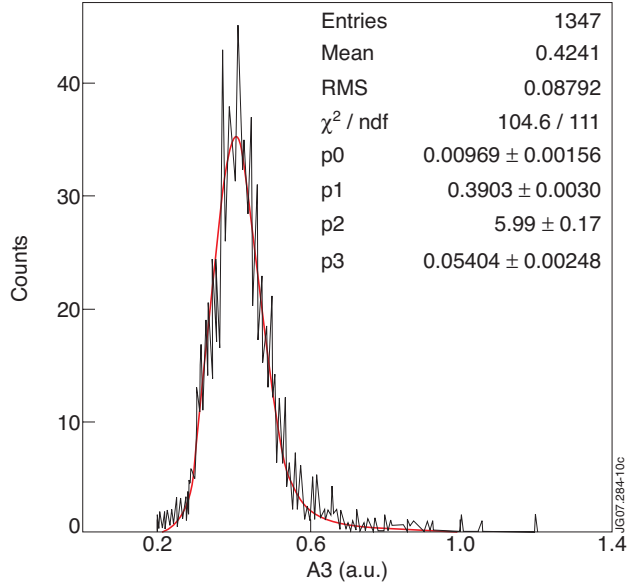
Figure 10: Example of measured amplitude distribution (A3) with PM1 tube in test 5 with the β_{min} radiation passing through the layers L1 and L2 of detector P/b at the mid point; also shown is Gaussian convoluted Landau distribution fitted to the data. The parameters p1 and p3 are the most probable value of the Landau distribution (μ) and the standard deviation of the Gaussian distribution (σ), respectively.
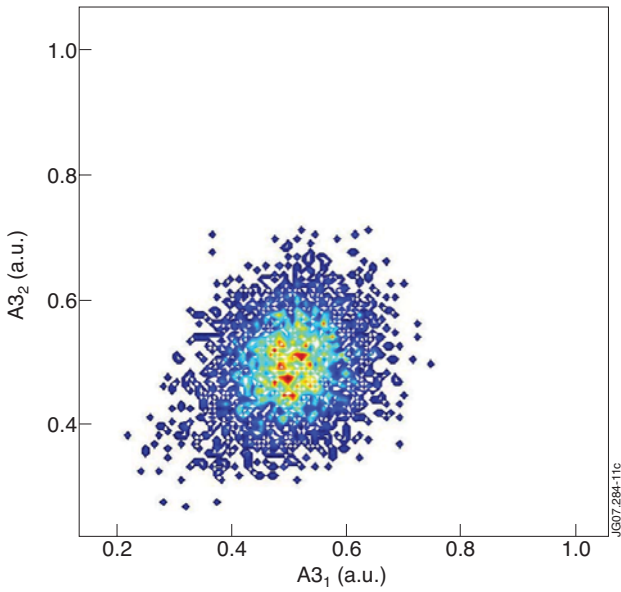
Figure 11: Contour plot of the measured event distribution as A3 amplitudes recorded with PM1 ($A3_1$) and PM2 ($A3_2$) tube in test 2 with α's impinging on L1 (BC-404) of the detector P/b.
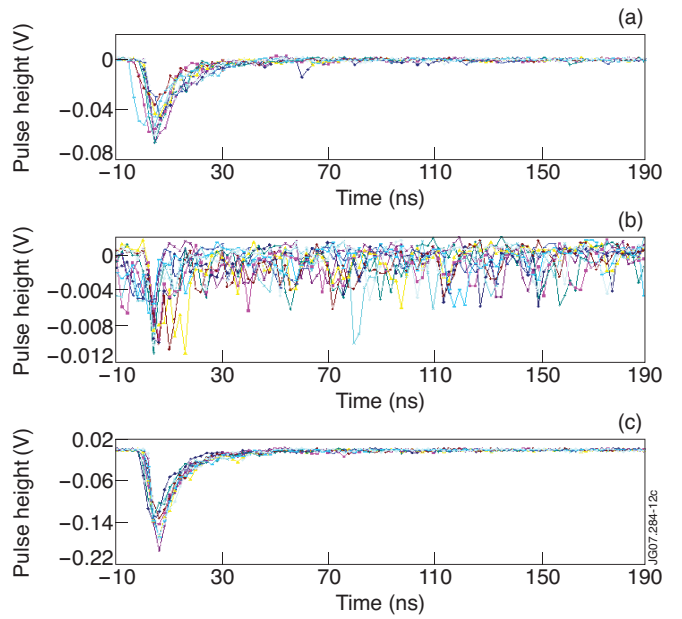
Figure 12: Examples of summed PM tube signals (PM1+2) in tests 1 and 2 with α's impinging on L1, (a), and L2, (b), of detector P, and L1 of P/b, (c).

29
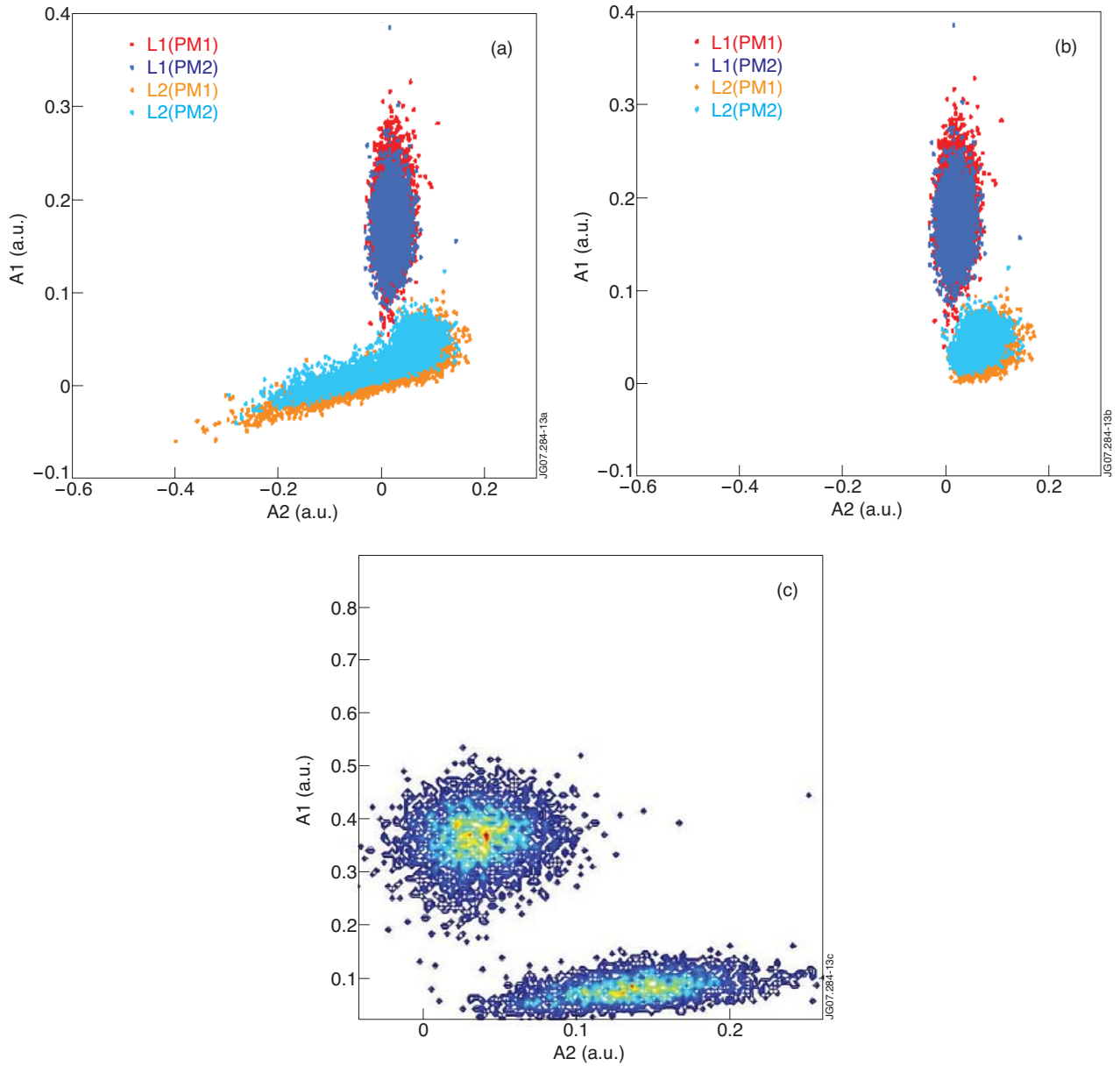
Figure 13: Scatter plots of the event distributions A1 vs. A2 recorded for a's impinging on L1 and L2 in test 1 for PM1 and PM2 individually (a and b) and PM1+2 (c); the L2 events shown in (b) were limited to those above the threshold of $A3_{th}=0.03a.u.$ (2823 events); the scatter plot (c) is shown as contours to displayed intensity distribution.
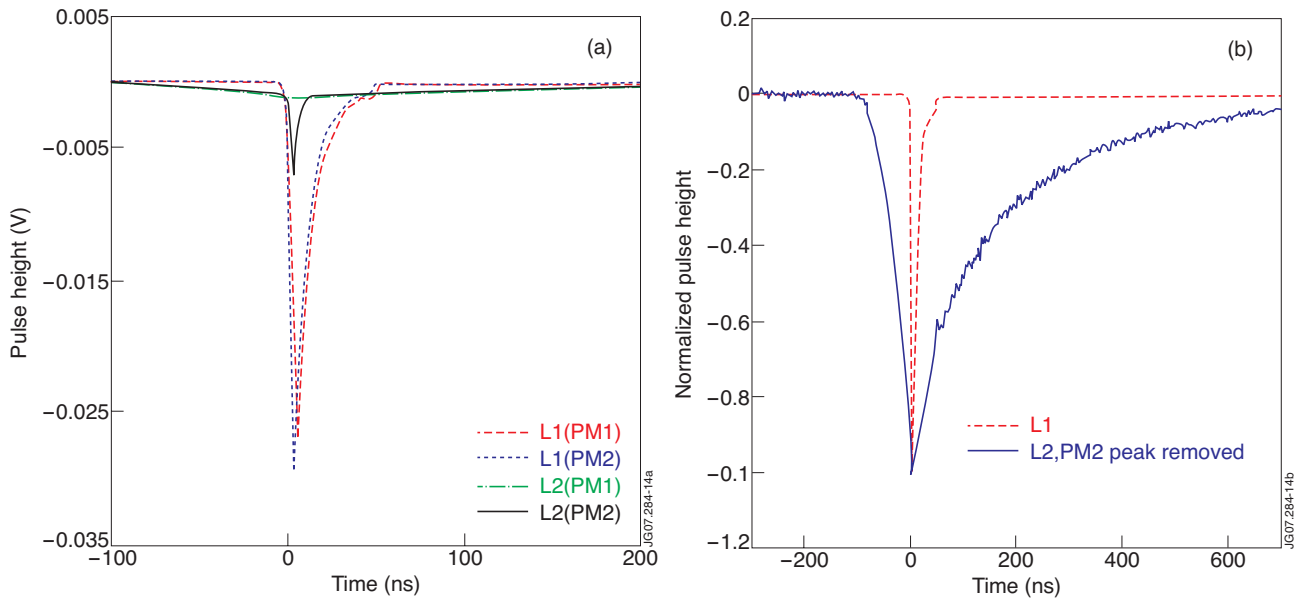
Figure 14: Average waveforms due to a interactions in L1 and L2 of detector P in test 1 for individual PM1 and PM2 data, (a), and PM1+2, (b), where the peak for L2 and PM2 has been removed; PM2 provided the trigger (see text).
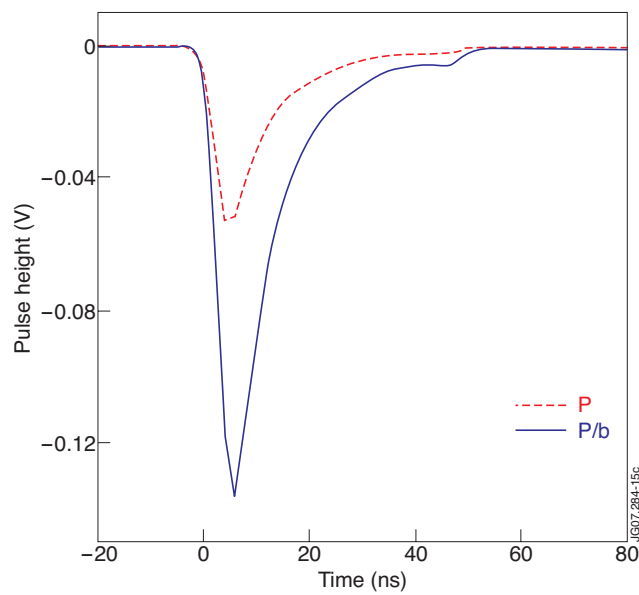
Figure 15: Average waveforms for a interactions in L1 of detectors P and P/b from data recorded with PM1+2.
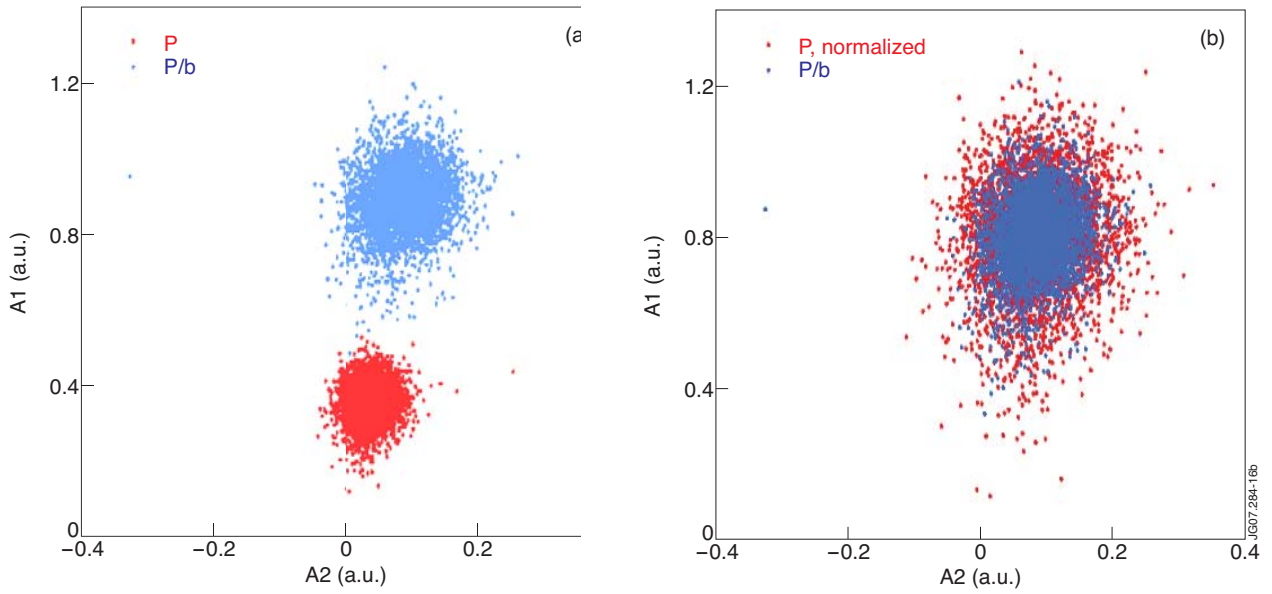
Figure 16: Amplitude distribution A1 vs. A2 of events due to a interactions in L1 of detectors P and P/b as measured, (a), and after normalization of the P data to the average amplitude A3 obtained from detector P/b, (b).
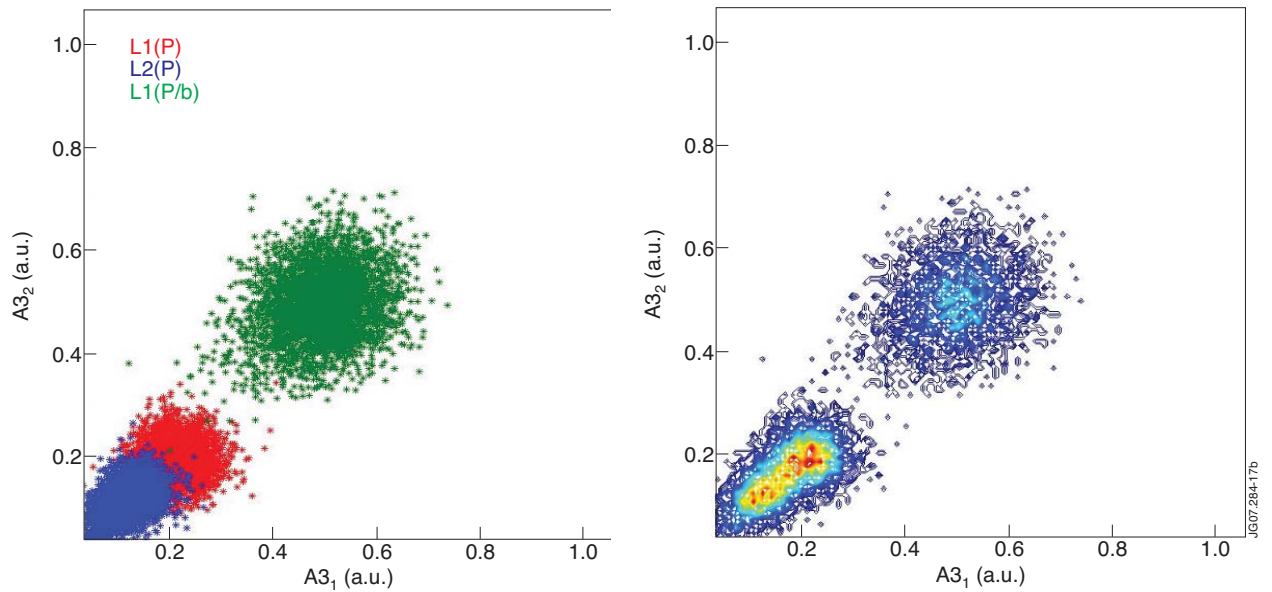
Figure 17: Scatter plot of A3 amplitudes recorded by PM1 ($A3_1$) and PM2 ($A3_2$) for α's in L1(P), L2(P) and L1(P/b) (left hand panel) and enhanced as contour plot on the right.
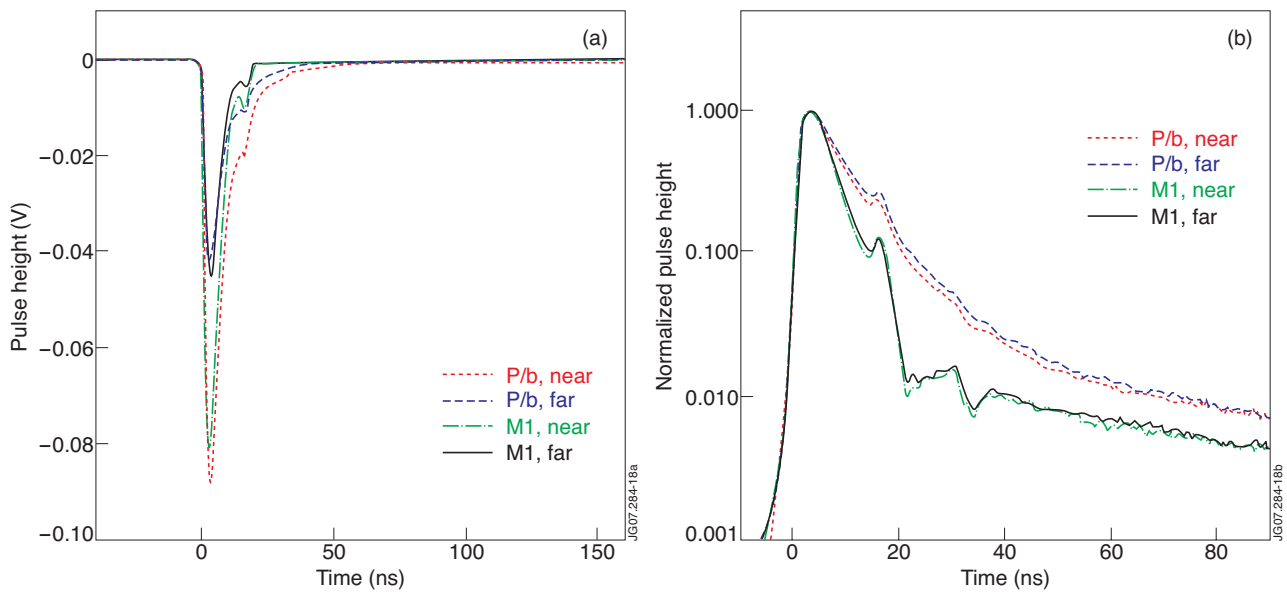
Figure 18: Comparison of average waveforms for a source positions in test 3 near and far away the PM tube of detectors P/b and M1 as measured (a) and after normalization at the peak value (b).
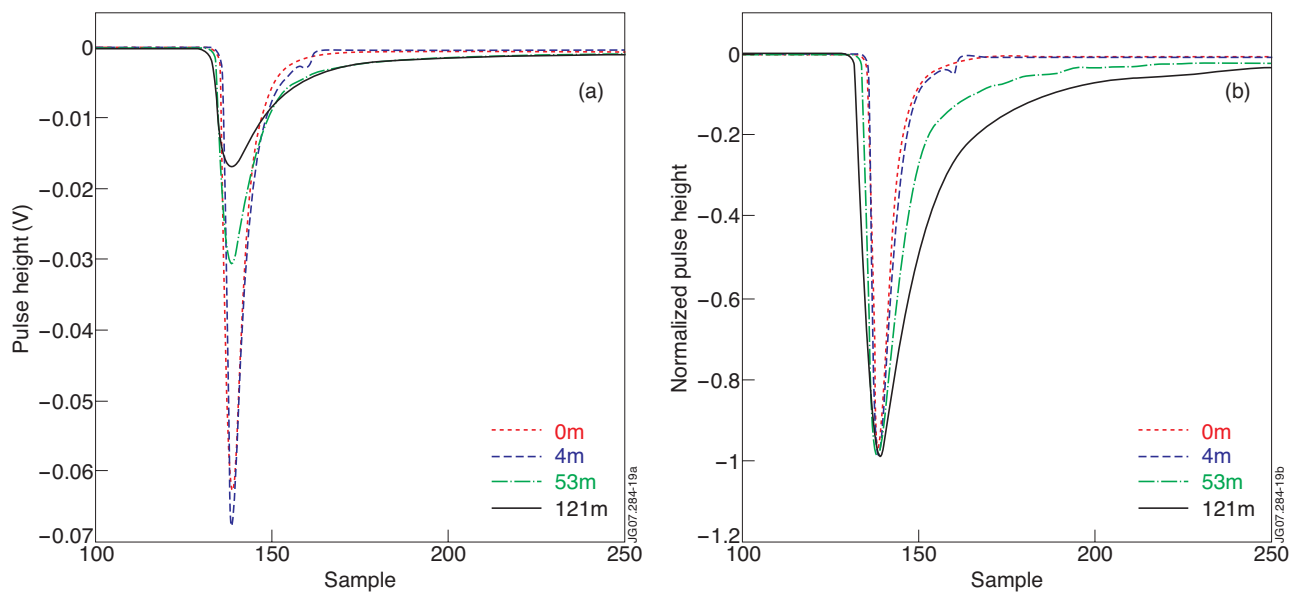
Figure 19: Average waveforms due to α's onto L1 of P/b recorded by PM1 in test 4 with RG-58 cables of different lengths as measured, (a), and after normalization to the peak value, (b).
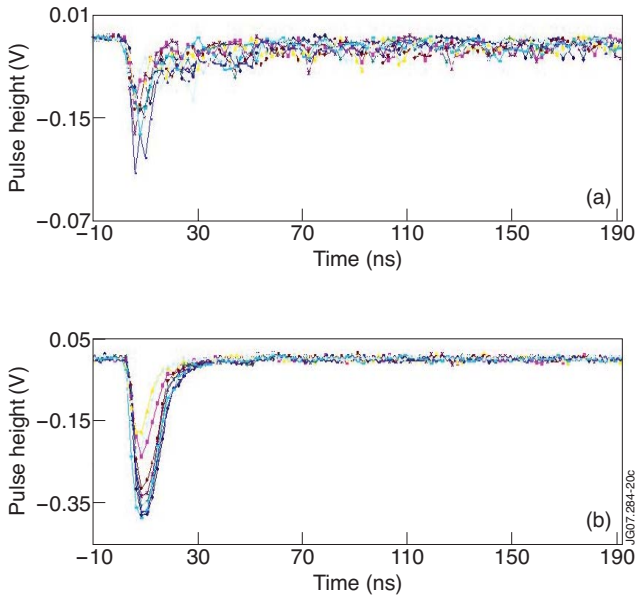
Figure 20: Waveforms of the β_{min} radiation on the midpoint of the P/b detector recorded with PM1+2, (a), and those of the corresponding trigger signal in detector C, (b)
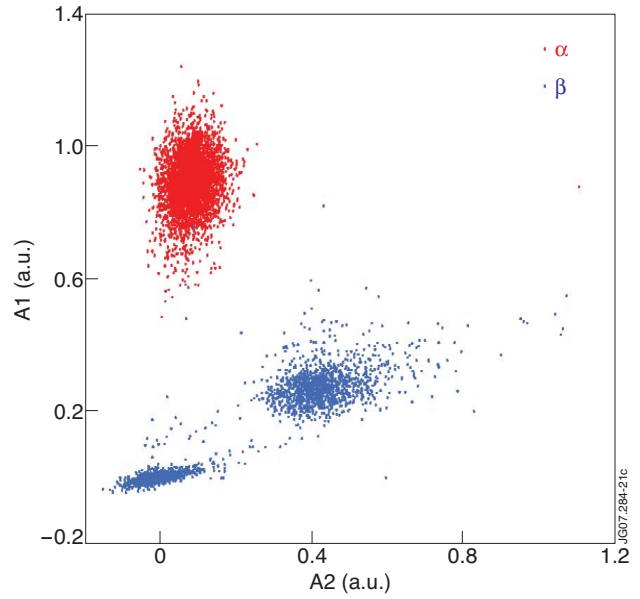
Figure 21: Comparison of scatter plot A1 vs. A2 for signals from the P/b detector recorded with PM1+2 for a and β_{min} radiation in tests 2 and 5. The centre of the distributions lies about A1/A2=0.9/0.1 and 0.25/0.4, respectively.
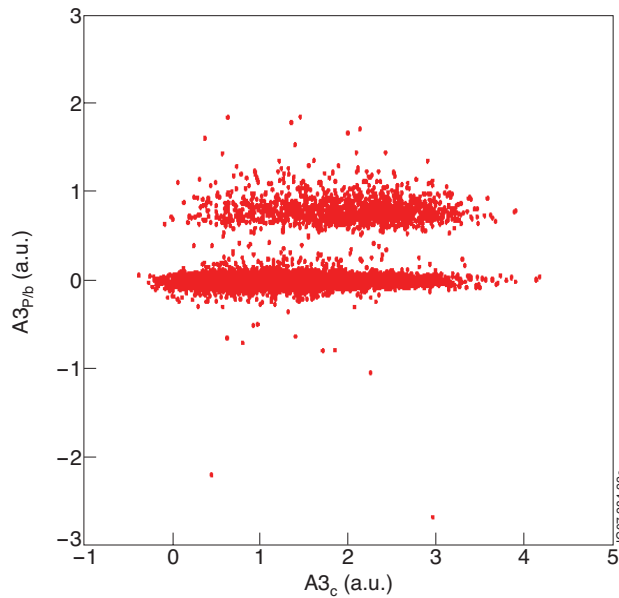
Figure 22: Scatter plot of $A3_{P/b}$ vs. $A3_C$ for data of test 5. The upper band of events are due to P/b-C detector coincidences generated by β_{min} and the lower band to accindentals which can be eliminated by a thereshold set at $A3_{th}$=0.2 a.u.
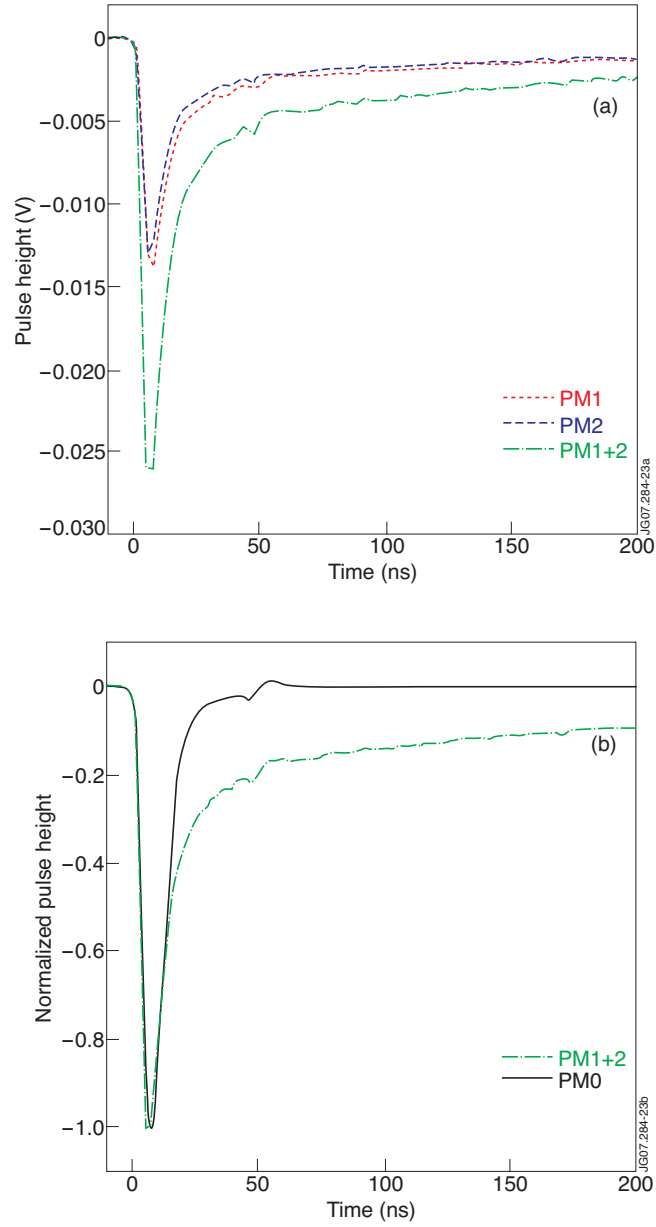
Figure 23: Results on average waveforms of β_{min} events in P/b as recorded by PM1, PM2 and PM1+2 signals, (a), and comparison of those of PM1+2 and PM0 of detector C (normalized by a factor 1/12) in (b).
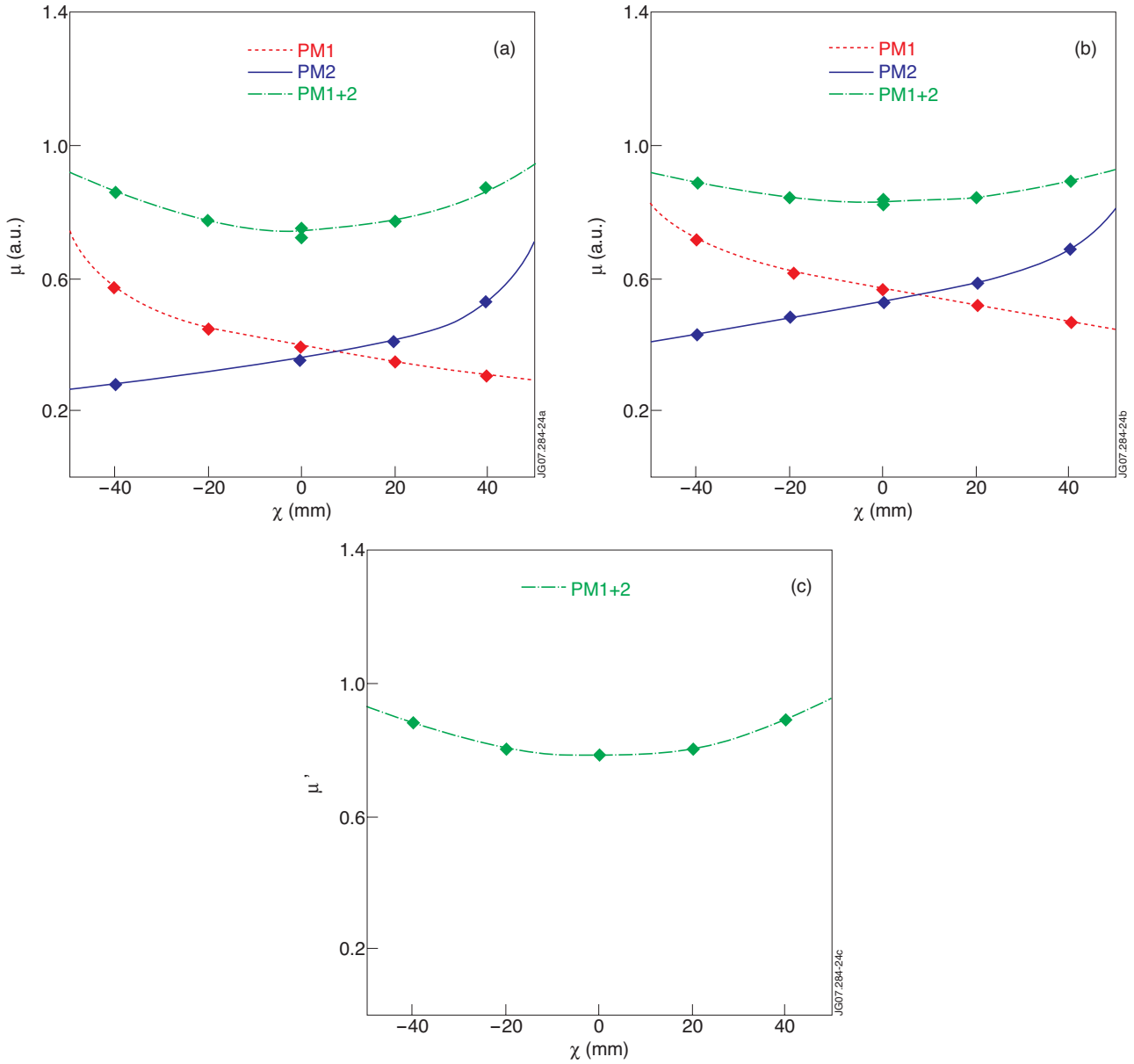
Figure 24: Results on the A3 response of detector P/b as function of longitudinal position of the β_{min} source, m(x), as recorded by PM1, PM2 and PM1+2 as measured, (a and b), and the sum PM1+2 after normalization to the same individual PM tube average value in x=0, (c). Also shown are double exponential fits to the data. The statistical errors shown are small.
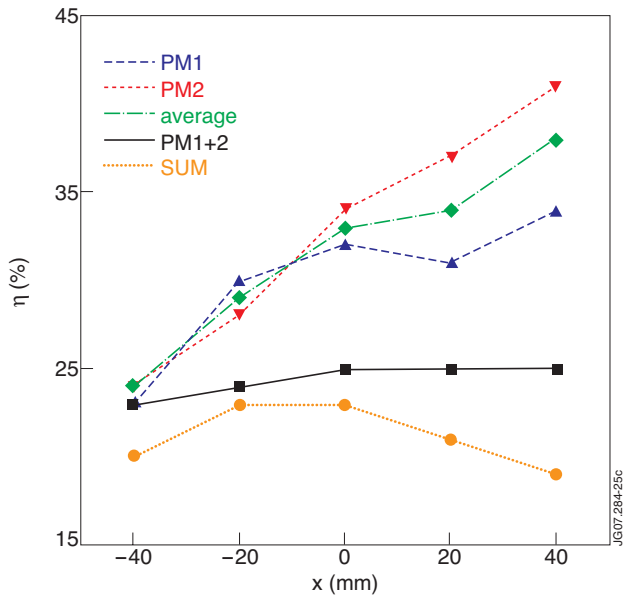
Figure 25: Results on pulse height resolution of detector P/b as function of β_{min} source longitudinal position, h(x), as recorded by PM1, PM2, their average, PM1+2 and the quadratic sum of h_1 and h_2 values (SUM).
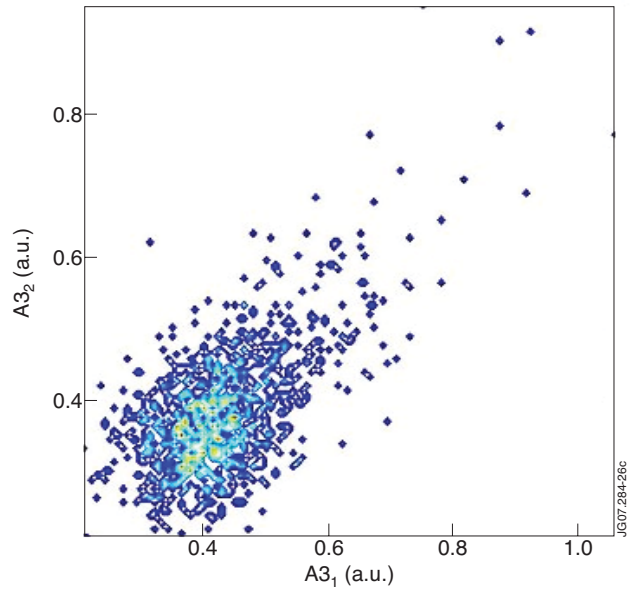
Figure 26: Contour plot of A3 amplitudes recorded by PM1 and PM2 for β_{min} radiation in the mid-point of the P/b detector.
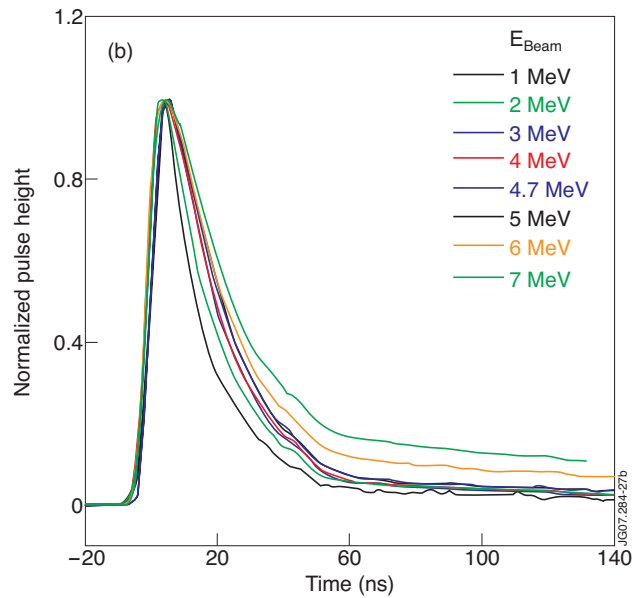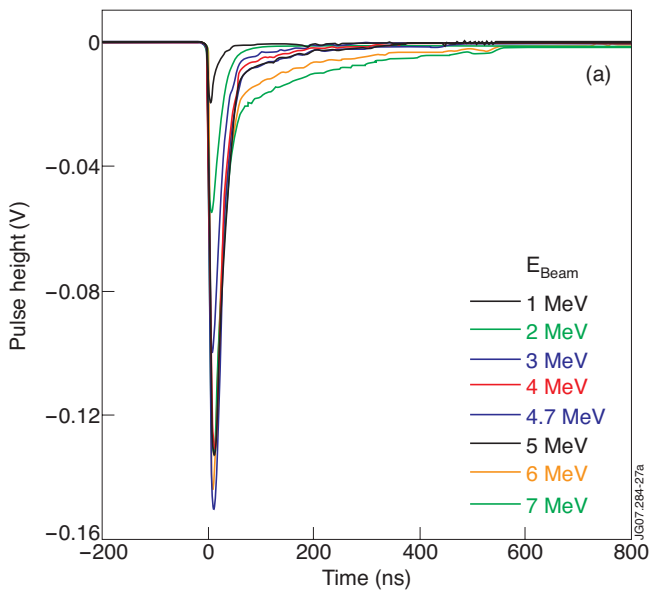
Figure 27: Average waveforms recorded by PM1 tube in test 6 for protons into the middle of detector P/b for different beam energies as measured, (a), and after normalization and truncated time scale, (b).
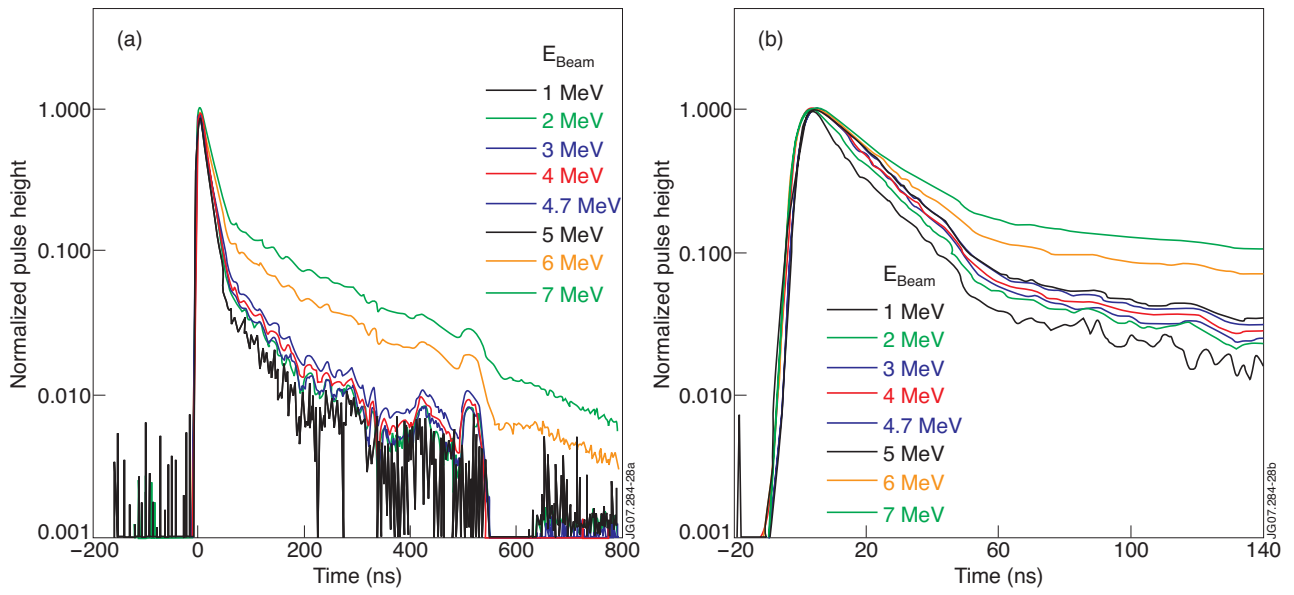
Figure 28: Same as Fig. 27b but in logarithmic scale.
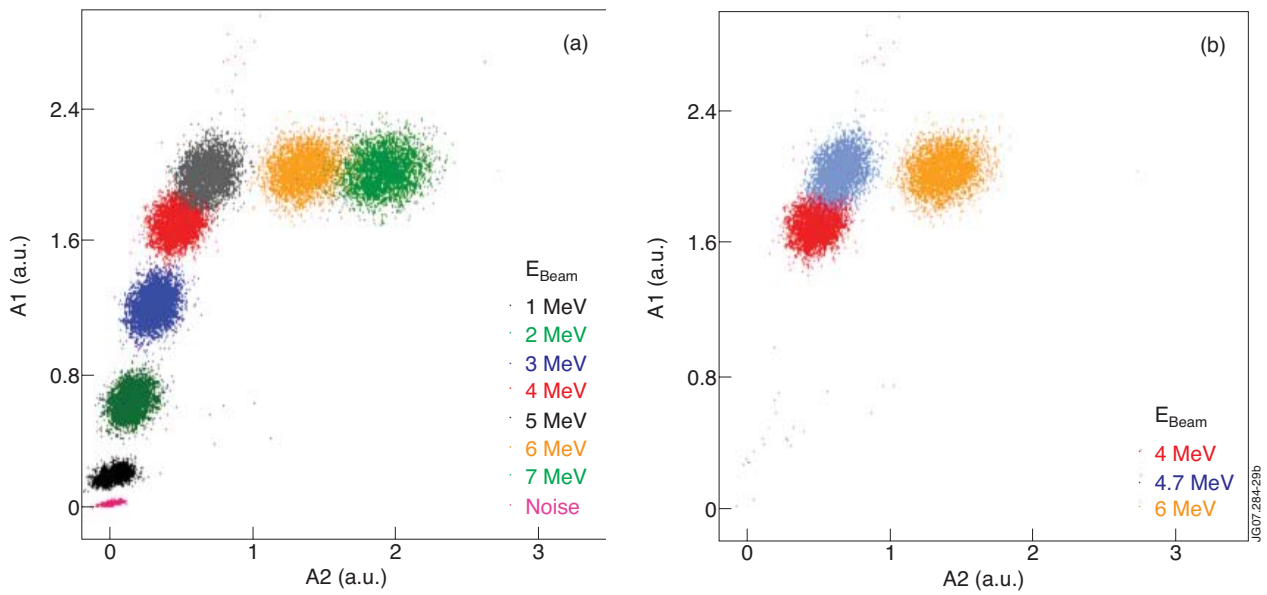
Figure 29. Scatter plots A1 vs. A2 for the data of test 6.
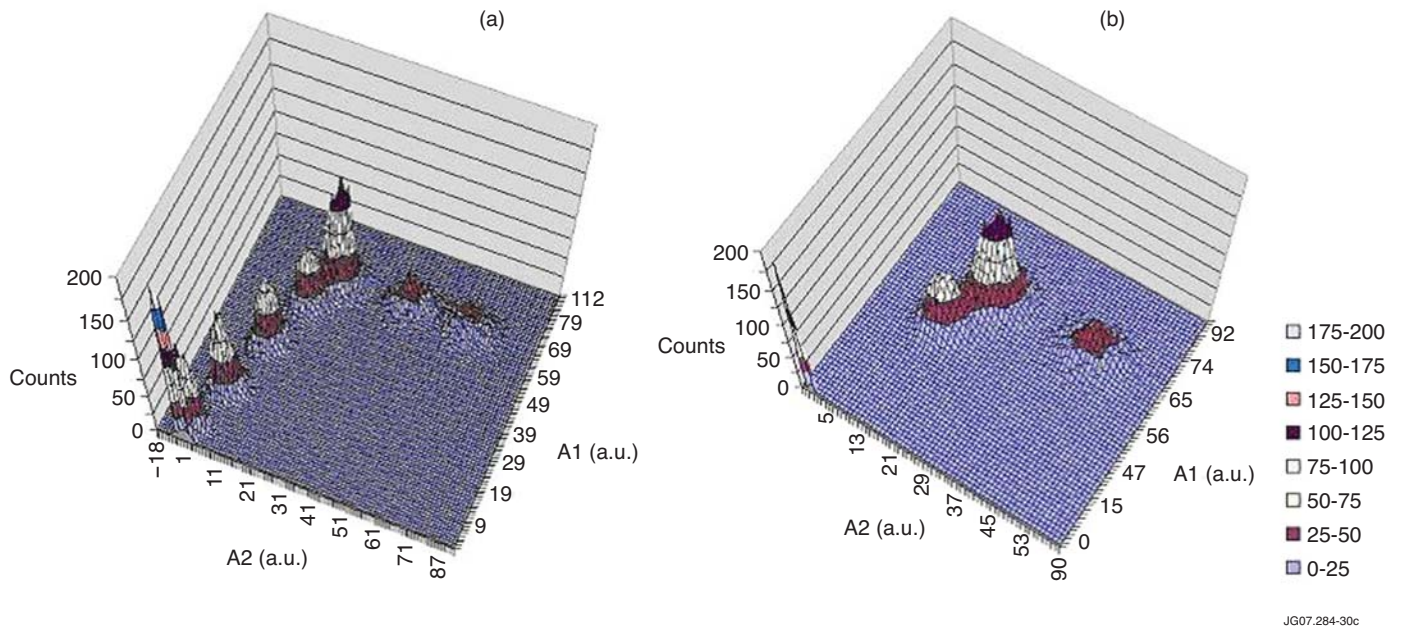
Figure 30: 3D representation of the A1 vs. A2 scatter plots of Fig 29.
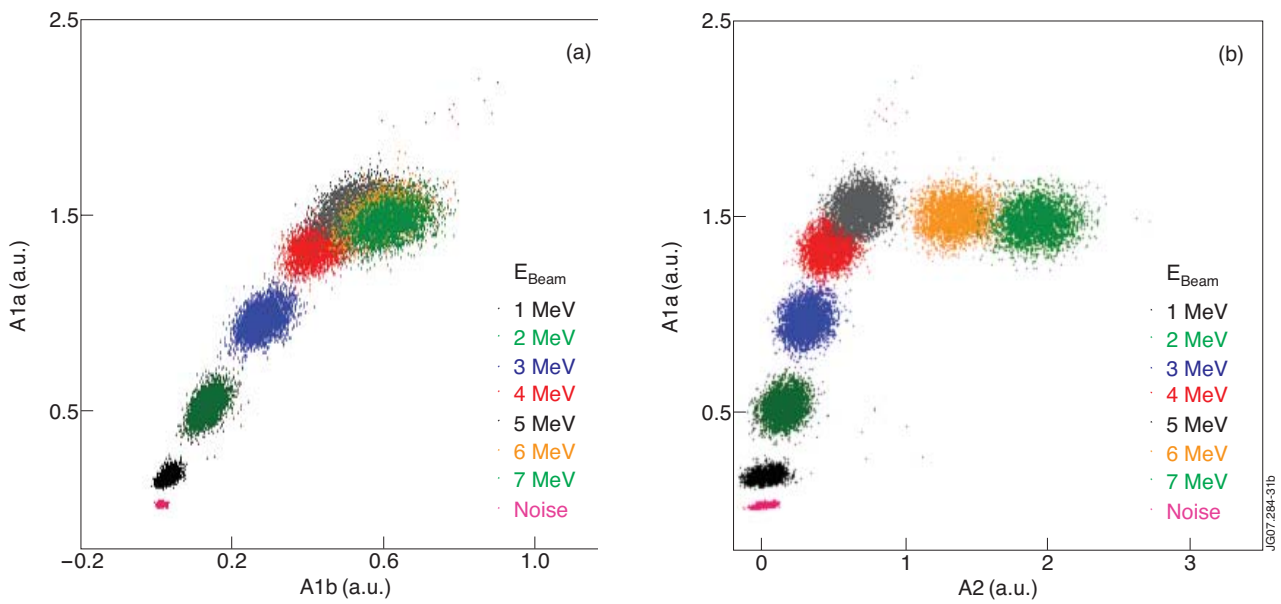
Figure 31: Comparison of waveform analyses of the data of test 6 using integration periods defined by the gates G1a, G1b and G2 and the results in terms of the scatter plots A1a vs. A1b, (a), A1a vs. A2, (b), A1b vs. A2, (c).
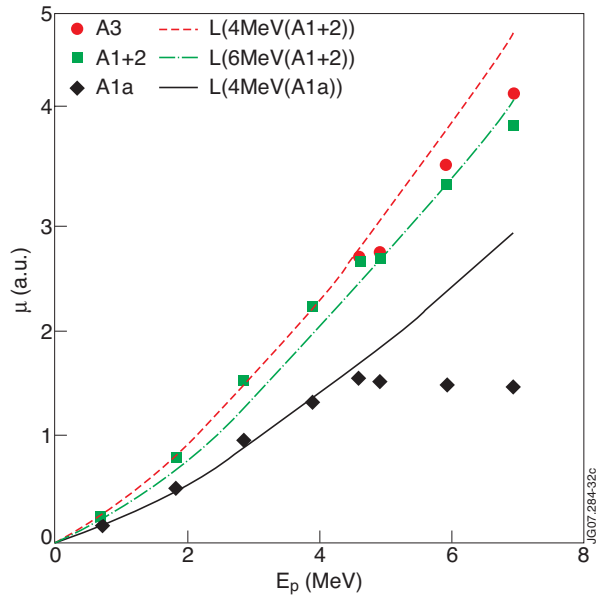
Figure 32. Amplitudes mean value as function of proton energy m(E_p) for the amplitude distributions A3, A1+2 and A1a from Table 11 compared with the calculated light yield functions L=f(E_p) normalized at E_{Beam}=4 MeV for A1a and A1+2 values and at E_{Beam}=6 MeV for A1+2 value.
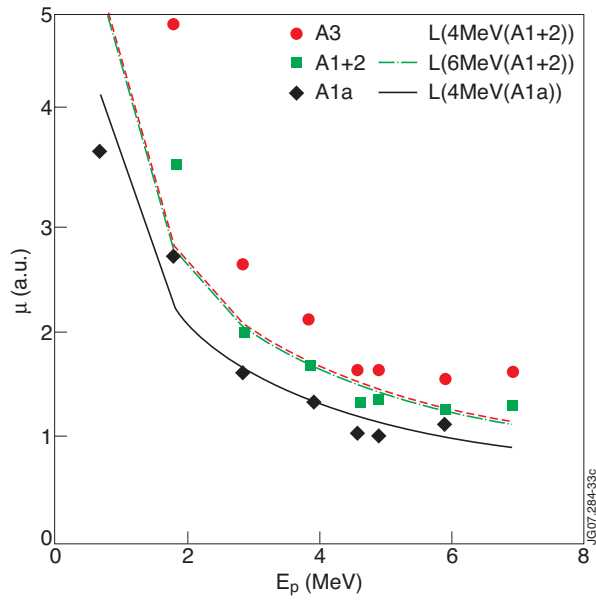
Figure 33: Pulse height resolution h as function E_p for the distribution of A3, A1+2 and A1a compared with the projected light yield curves L(E_p) normalized as for Fig. 32.
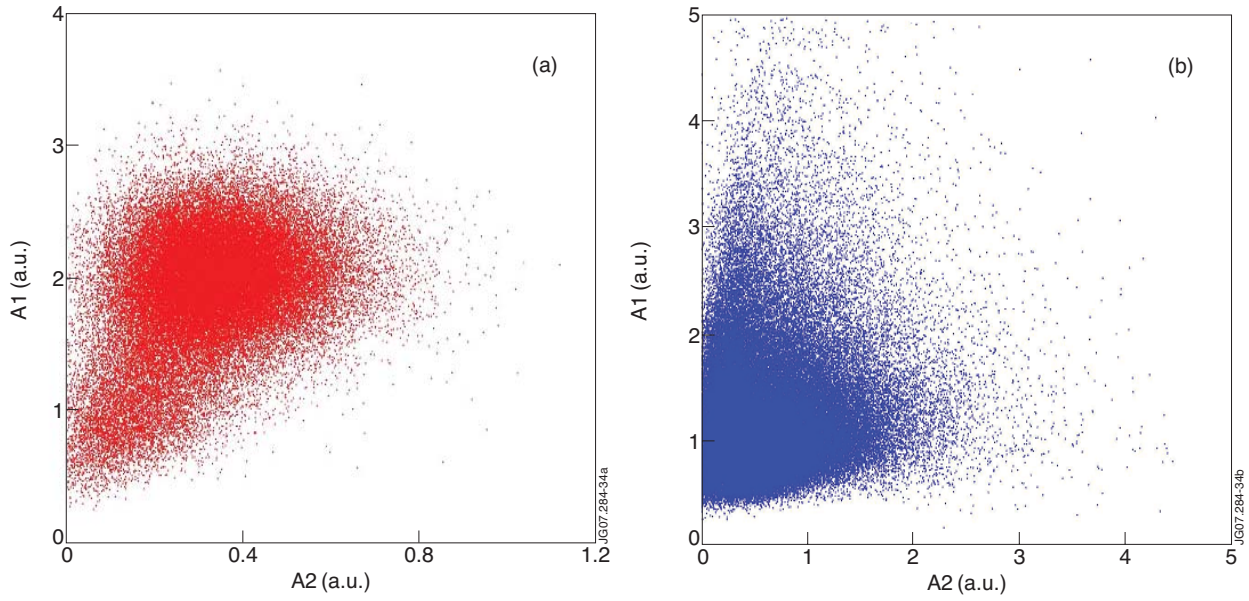
Figure 34: Scatter plots of A1 vs. A2 amplitudes for α, (a), and β, (b), signals from detector P/b recorded with PM1 tube in test 7a.
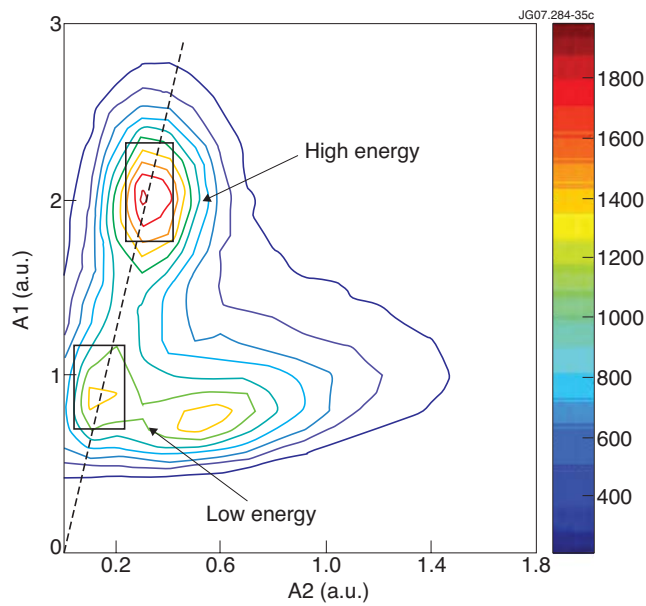
Figure 35: Contour plot of A1 vs. A2 of the superposition of the a and b distributions in Fig. 34. The events falling within the upper and lower boxes indicated are identified as due to high and low energy particle deposition in L1 of detectors P/b assumed to fall along the line A1-7A2=0 (indicated).
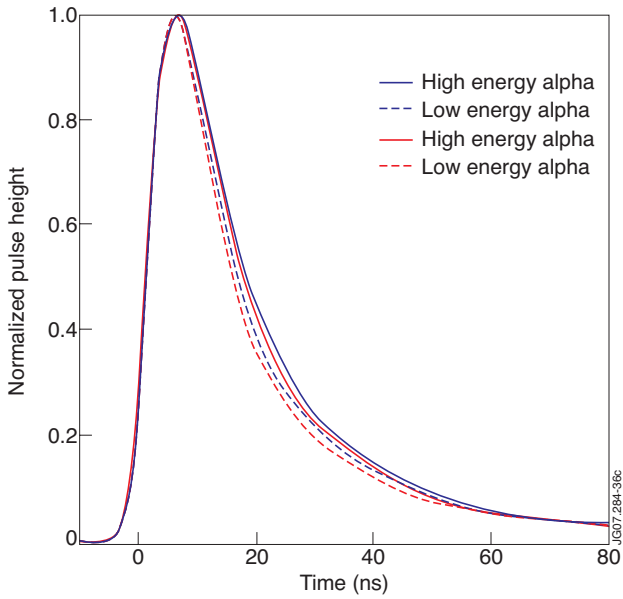
Figure 36: Average waveforms for high and low energy α's and β's depositing their energy in L1 (BC-404) of the P/b detector recorded by PM1 tube in test 7a; normalization at the peak value has been applied
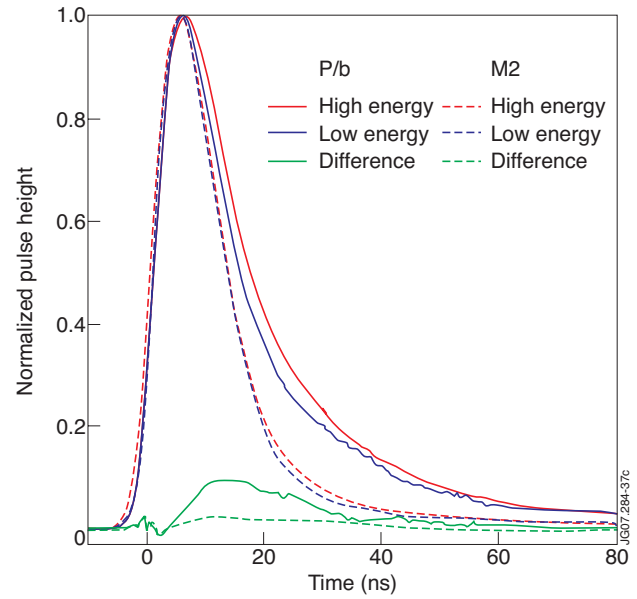
Figure 37: Average waveforms for high and low energy β's depositing their energy in L1 (BC-404) of the P/b phoswich detector and in the monolithic detector M2 recorded by PM1 tube in test 7b; normalization at the peak value has been applied. The high and low energy pulse difference for the two detectors is also shown.
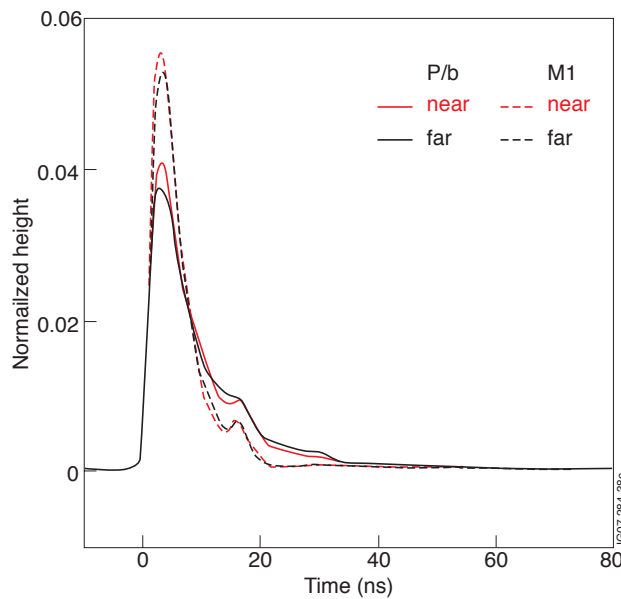

Figure 38: Average waveforms recorded with PM1 tube for detectors P/b and M1 with the a source placed at the near and far end relative to the PM tube (test 3). The waveforms were normalized so as to give the same value for the A1 amplitude.
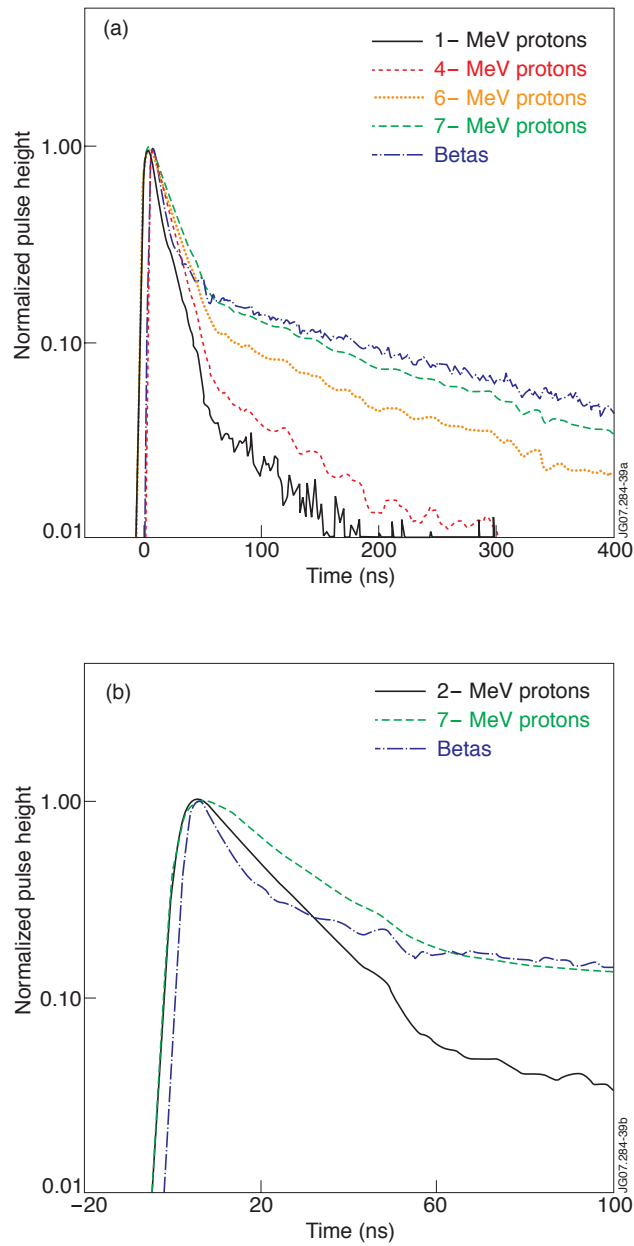
42

Figure 39: Comparison of the average waveforms recorded with PM1 tube for detector P/b with protons of E_{Beam} = 1, 4, 6 and 7 MeV (test 6) and β_{min} radiation (test 5) as measured, (a), and detailed comparison of 2 and 7-MeV proton and β_{min} results normalized at the peak value, (b).
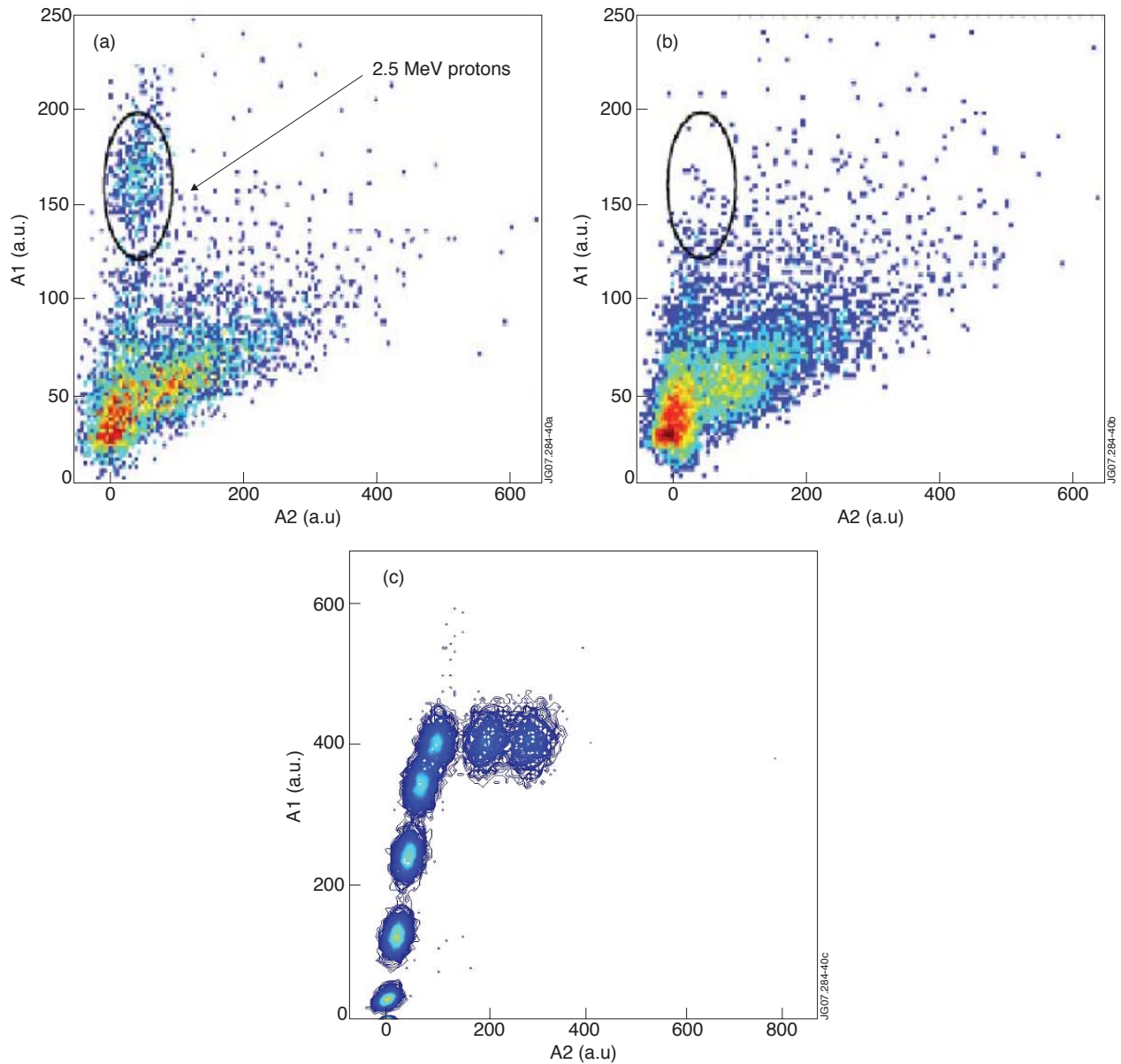
Figure 40: Example of measured A1-A2 scatter plot with a central phoswich scintillator in the focal plane hodoscope mounted in the MPRu spectrometer installed at JET in December 2004. The data obtained with the MPRu spectrometer set to record 2.5MeV recoil protons from neutrons emitted in deuterium plasmas, (a), and set to zero magnetic field to record background radiation only, (b), adapted from [26]. Comparison is made with contour plot relative to the proton beams of different energies, (c), of test 6 as shown also in Fig.29a.